THESIS FOR THE DEGREE OF LICENTIATE OF ENGINEERING IN THERMO AND FLUID DYNAMICS

Numerical Methods for Aeroacoustic Analysis of Turbomachinery

DANIEL LINDBLAD

Department of Mechanics and Maritime Sciences
CHALMERS UNIVERSITY OF TECHNOLOGY

Göteborg, Sweden 2018

Numerical Methods for Aeroacoustic Analysis of Turbomachinery
DANIEL LINDBLAD

Thesis for the degree of Licentiate of Engineering 2018:14
Department of Mechanics and Maritime Sciences
Chalmers University of Technology
SE-412 96 Göteborg
Sweden
Telephone: +46 (0)31-772 1000

Chalmers Reproservice
Göteborg, Sweden 2018

Numerical Methods for Aeroacoustic Analysis of Turbomachinery
Thesis for the degree of Licentiate of Engineering in Thermo and Fluid Dynamics
DANIEL LINDBLAD
Department of Mechanics and Maritime Sciences
Chalmers University of Technology

Abstract

Air transportation is today an integral part of many peoples life and it continuously grow to serve more of us in new and ingenious ways. There are however negative sides to this growth as well, such as increased noise around airports and more CO_2 emissions, which must be addressed if aviation is to be part of a sustainable future. A key ingredient to successfully addressing these issues is accurate and reliable numerical tools that can be used to investigate and/or optimize new and existing technologies.

This thesis presents a computational framework for predicting the noise generated by a fuel efficient aircraft engine propulsor known as the Counter Rotating Open Rotor (CROR). The framework solves the Favre-Averaged Navier Stokes equations using the Finite Volume method for spatial discretization and the Harmonic Balance method for temporal discretization in order to obtain a numerical solution of the transient flow field around the CROR blades. This solution is further coupled with an acoustic analogy in which a convective form of the Ffowcs Williams-Hawkings equation for permeable integration surfaces is used to determine the far field noise signature of the CROR at any arbitrary observer location. The underlying theory of both the temporal discretization scheme (Harmonic Balance method) and the acoustic analogy (Ffowcs Williams-Hawkings equation) are presented in detail in order to investigate the applicability of these methods for predicting CROR noise. It is found that the Harmonic Balance method performs well for predicting turbomachinery noise in general, but also that issues with aliasing might impair the accuracy of the results when the flow-field becomes strongly nonlinear. The acoustic analogy is found to perform well for propagating the types of noise generated by a CROR. Issues may however occur when wakes and shock waves cross the integration surface. This makes the placement of the integration surface a complicated task for the particular formulation of the Ffowcs Williams - Hawkings equation used in this work.

Keywords: Computational Aeroacoustics, CAA, Tonal Noise, Counter Rotating Open Rotor, Harmonic Balance Method, Von Neumann Stability Analysis, Acoustic Analogy, Convective Ffowcs Williams - Hawkings Equation

To my family, for always believing in me.

"Det finns inga genvägar fram till det perfekta ljudet"

- Farbror Barbro

"There are no shortcuts for obtaining the perfect sound"

Acknowledgements

Pursuing a Ph.D. proved to be a very challenging task on both a technical and personal level. This journey would therefore not have been possible without all the great people that have surrounded me and provided me both technical and emotional support along the way.

I would like to start by expressing my deepest gratitude to my supervisor Niklas Andersson, for giving me the freedom to explore the interesting field of Computational Aeroacoustics, and for helping me solve a great deal of problems that I have encountered along the way. I would also like to acknowledge my colleagues at the department of Mechanics and Maritime sciences for making work such a fun and inspiring place to be. A special thanks to Gonzalo, for the fun, productive and completely unproductive sessions that we have had, to Alexandre, for helping me understand propellers, to Carlos for giving me a lot of good advices and support, and to Guglielmo, for the all the fun and competence you have brought to our office. I would also like to thank my family for all the support that you have provided me throughout my life, and Darya, for they joy you have brought into my life.

This work was funded by the E.U. under the ULTIMATE[1] Project funded by the European Commission within the Horizon 2020 Programme (2014-2020), Grant Agreement No 633436. This financial support is gratefully acknowledged. I would also like to express my gratitude to all partners of the ULTIMATE project who have contributed to the work reported in this thesis. The computer resources provided by the Swedish National Infrastructure for Computing (SNIC) at the National Supercomputing Centre (NSC) in Linköping, Sweden and Chalmers Centre for Computational Science and Engineering (C^3SE) in Gothenburg, Sweden, are also gratefully acknowledged.

[1] Ultra Low emission Technology Innovations for Mid-century Aircraft Turbine Engines

Nomenclature

Greek Letters

$\delta(x)$	Dirac delta function	
δ_{ij}	Kronecker delta	
ε_n	Time spectral viscosity coefficient for the n^{th} harmonic	s
λ	Eigenvalue to flux Jacobian	m s^{-1}
Λ^*	Matrix containing eigenvalues to flux Jacobian along diagonal	
ξ_n	Eigenvalue to D corresponding to the n^{th} harmonic	s^{-1}
ρ	Density	kg m^{-3}
σ_{ij}	Viscous stress tensor	kg m^{-1} s^{-2}
τ	Pseudo time	s
τ_{ret}	Retarded time/emission time	s
$\phi(\mathbf{x})$	Test function	
ϕ	Normalized spatial wavenumber	rad
ψ	Normalized angular frequency	rad
ω_n	Angular frequency of n^{th} harmonic	rad s^{-1}

Roman Letters

c	Speed of sound	m s^{-1}
D	Time spectral derivative matrix	s^{-1}
$\mathcal{F}_j$	Vector containing total flux of conserved variables	
$\mathcal{F}_j^*$	Vector containing total flux of conserved variables for all time levels	
$G(\mathbf{x}, t)$	Green's function to convective wave operator	
$\hat{h}_n$	Eigenvector to D corresponding to the n^{th} harmonic	
$\mathcal{H}$	Vector containing source terms	
$\mathcal{H}^*$	Vector containing source terms for all time levels	
$H(x)$	Heaviside step function	
k_j	Spatial wavenumber	rad m^{-1}
$\tilde{L}_i$	Momentum source term in generalized momentum equation	kg m^{-2} s^{-2}
L_i	Source term in the convective Ffowcs Williams - Hawkings equation	kg m^{-2} s^{-2}
M	Mach number	
N_h	Number of harmonics	
N_t	Number of time levels	

N_{var}	Number of conserved variables	
n_i	Cartesian component of surface normal vector	
p	Static pressure	kg m s^{-2}
p_{ij}	Compressive stress tensor	kg m^{-1} s^{-2}
$\hat{\mathcal{Q}}_n$	Fourier coefficient vector for n^{th} harmonic	
$\mathcal{Q}$	Vector containing conserved variables	
$\mathcal{Q}^*$	Vector containing conserved variables for all time levels	
Q	Mass source term in generalized continuity equation	kg m^{-3} s^{-1}
T	Time period	s
T^*	Matrix containing eigenvectors to flux Jacobian	
T_{ij}	Lighthill tensor	kg m^{-1} s^{-2}
t	Time	s
$\hat{u}^m$	Fourier coefficient for a single spatial-temporal mode at pseudo time instant m	
u_i	Cartesian component of velocity vector	m s^{-1}
V	Time spectral viscosity matrix	s^{-1}
$\mathcal{W}^*$	Vector containing characteristic variables for all time levels	
$\mathbf{x}$	Position vector	m
x_j	Cartesian component of position vector	m
$\mathbf{y}$	Position vector of acoustic source	m

Superscripts and Subscripts

$\square'$	Perturbation from observer state
$\square^T$	Transpose
$\square_0$	Observer state or mean state

Thesis

This thesis consists of an extended summary and the following appended papers:

Paper A D. Lindblad and N. Andersson. "Validating the Harmonic Balance Method for Turbomachinery Tonal Noise Predictions". *55th AIAA Aerospace Sciences Meeting*. AIAA Paper 2017-1171. Grapevine, TX, 9-13 January 2017

Paper B D. Lindblad et al. "Aeroacoustic Analysis of a Counter Rotating Open Rotor based on the Harmonic Balance Method". *2018 AIAA Aerospace Sciences Meeting*. AIAA Paper 2018-1004. Kissimmee, FL, 8-12 January 2018

Contents

Part I
Extended Summary

1 Introduction

Modern transportation systems have become an integral part of many peoples life and continuously evolve to serve more and more of us in new and ingenious ways. Today, people from all around the globe have the ability to meet, explore other cultures and exchange goods within time frames that probably were not even dreamt about by our ancestors. This change in mobility has partly been enabled by the air transportation sector, which has grown over the past half-century into what is today a safe, efficient and global transportation system. In the future, air transport is also expected to continue growing at a rate of approximately $4 - 5\%$ per year[1]. In the long term, this rate could lead to a global increase in air traffic of about 7 times between the years 2010 and 2050 [4]. In response to this expected growth the European Union has formulated its vision for a sustainable aviation future, called "Flightpath 2050" [5]. Among many things, this document states that the CO_2 emissions and perceived noise levels from aircrafts in 2050 respectively should be 75% and 65% lower than year 2000 levels. In order to meet these goals the Advisory Council for Aviation Research and Innovation in Europe (ACARE) has developed the Strategic Research and Innovation Agenda (SRIA) [6]. The strategy in SRIA for meeting the noise targets of Flightpath 2050 are very much in line with the "Balanced Approach" for aircraft noise management set forward by ICAO [4], which is the United Nations organ that, among many things, develops guidelines for aircraft noise certification. In the Balanced Approach, reduction of noise at source (aircraft) is emphasized as an important strategy for minimizing the noise impacts of aviation. Reducing the noise at source should, according to the SRIA targets, be achieved by both developing new, revolutionary noise reduction technologies as well as by improving (evolving) already existing ones. In either of these cases, ACARE identifies further development of numerical simulation tools as a key ingredient in this process.

The purpose of this thesis is to make a contribution to the SRIA targets by further developing and analyzing a numerical tool used at Chalmers University of Technology for aircraft engine noise predictions, called G3D::Flow. In particular, the work reported in this thesis has been focused on setting up a computational framework for predicting the noise generated by Counter Rotating Open Rotor (CROR) fan blades, see figure 1.1. The CROR engine is characterized by its ultra high bypass ratio (BPR), which is defined as the ratio between the amount of air that only goes past the fan blades, called the bypass flow, to the amount of air that goes through the core of the engine, called the core flow. Increasing the BPR of Turbofan engines, see figure 1.2, has been an ongoing trend among aeroengine manufacturers for the past 40 years. The main motivation for doing this is that larger fans, which have a higher BPR, can operate with a lower fan pressure ratio while still generating the same amount of thrust. Lower fan pressure ratio does in

[1] Increase in revenue passenger kilometers globally. Prediction made for years 2017-2036. [3]

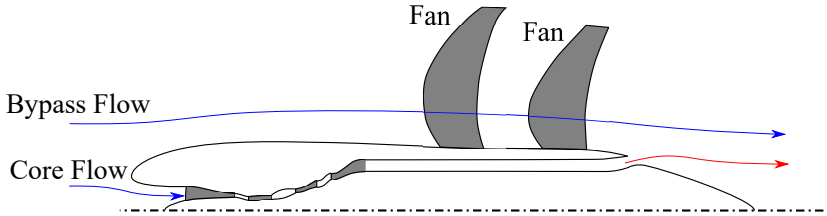

Figure 1.1: *Schematic View of a Counter Rotating Open Rotor Engine.*

turn give a lower exhaust velocity, which increases the propulsive efficiency of the engine and decreases the noise generated by the exhaust jet [7, 8]. Increasing the size of the fan does however also require a larger surrounding nacelle that will add weight to the engine and generate more aerodynamic drag. These penalties will eventually offset the efficiency gained from the higher BPR, which motivates the introduction of unducted propulsors such as the CROR. Removing the nacelle will however also enable the noise generated by the fan blades to propagate directly into the surrounding atmosphere. In the next section the underlying mechanisms that generate this type of noise will be explained in brief.

1.1 Noise Generation in a Counter Rotating Open Rotor

In order to define the noise generating mechanisms found in a CROR the flow field in the vicinity of the fan blades must first be understood. Consider therefore the flow along a stream surface that passes over one of the rotor blades as illustrated in figure 1.3. This picture can be obtained by looking at the flow on an axial/tangential plane that goes along the line denoted "Bypass Flow" in figure 1.1. From figure 1.3 it can be seen that a low pressure and a high pressure zone establishes around the suction and pressure side of the blade respectively. In the particular case depicted in this figure the flow is also transonic, which leads to the formation of a sharp discontinuity in pressure, known as a shock wave, close to the suction side's trailing edge. Figure 1.3 also illustrates how the slow moving fluid close to the blade, known as the boundary layer, forms a wake as it leaves the blade and continues to travel downstream.

The fact that the flow field illustrated in figure 1.3 is nonuniform is also the reason to why the fan blade generates noise. To see this, consider a stationary observer that

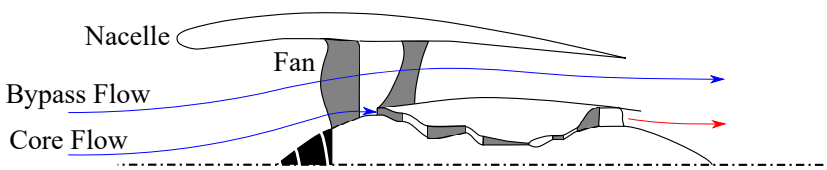

Figure 1.2: *Schematic View of a Turbofan Engine.*

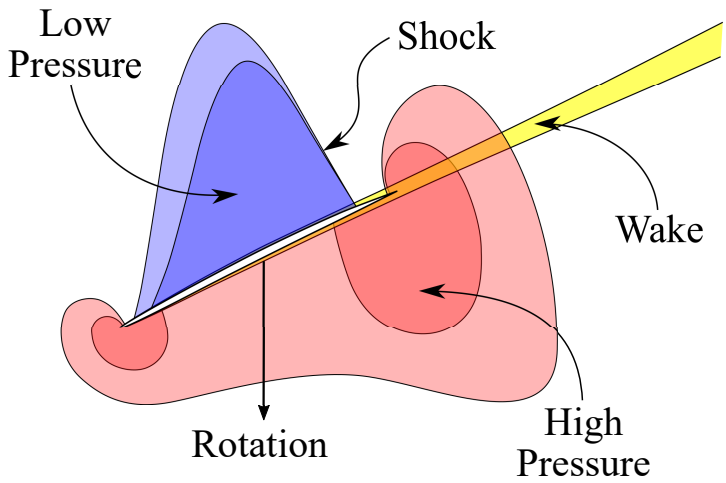

Figure 1.3: *Pressure Field and Boundary Layer generated by a Transonic Fan Blade.*

is located (for example) in front of the rotating fan. Naturally, the nonuniform pressure field around the blades will cause a variation in pressure at the location of the observer each time a blade sweeps by. This example illustrates that a rotating fan indeed gives rise to noise, but unfortunately does not provide much details about the underlying mechanisms that generates the pressure variations. The answer to this was provided in a famous publication by Ffowcs Williams and Hawkings [9]. The theory presented by these authors shows that a moving surface gives rise to three fundamental sources of noise: monopoles, dipoles and quadropoles. A nice illustration of how these noise sources arise for the specific case when the surface is a moving blade is further presented in [10]. In the latter work the monopole is identified as the source of noise coming from the volume displacement of air due to the periodic passing of the blades. The dipole noise is on the other hand generated by the uneven pressure field that develops around the blade as a result of its motion through the fluid, i.e. due to inviscid aerodynamic forces. Both these sources generates noise at frequencies which are multiples of the frequency with which the blade rotate. Noise at other frequencies can also be generated by the aforementioned mechanisms due to pressure fluctuations on the blade surface caused by either a turbulent boundary layer or ingestion of turbulence generated by for example an upstream bladerow into the fan. This turbulence induced noise is mostly generated close to the leading and trailing edge of the blade [10]. The mono and dipole noise sources are concentrated to the blade surfaces. The noise generated by the flow exterior to the surface and the effects that this flow has on noise propagation will finally be accounted for by the quadropole source. Here, the effects of the shock wave in figure 1.3 will for example appear.

An important factor that has to be taken into account when the noise generated by a CROR is calculated is the influence that the two fans have on each other [10]. Wakes generated by the upstream will for example impinge on the downstream blades as illustrated in figure 1.4. Pressure fluctuations generated by the downstream blades will

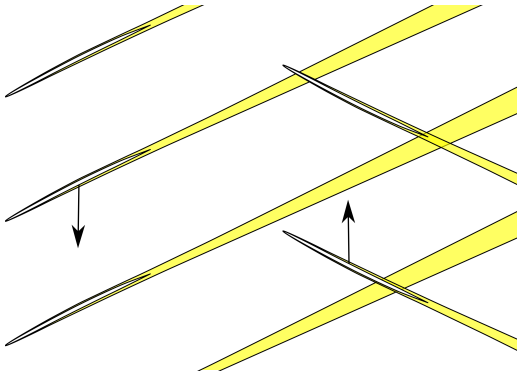

Figure 1.4: *Schematic View of Wake-Rotor Interaction in a CROR.*

also travel upstream and impinge on the upstream fan. In either of these cases the flow field around the blades will be altered, thus changing the noise signature of the CROR compared to if the blades would operate in isolation. It is however important note that this interaction does not produce new sources of noise, it only changes the amplitude and frequency of the aforementioned sources.

All noise sources except those caused by turbulent fluctuations are accounted for by the computational framework that will be presented in this thesis. The framework consist of two fundamental parts, namely a source prediction part and a noise propagation part. The theory connected to each of these two parts will be presented in Chapters 2 and 3 respectively. The aim of the source prediction part is to explicitly compute the flow field, i.e. noise sources, generated by a CROR by means of unsteady Computational Fluid Dynamics (CFD) simulations. In the noise propagation part, the sources computed in the CFD simulation are extracted and used to calculate the far-field pressure signal using a method based on the theory of Ffowcs Williams and Hawkings [9].

1.2 Purpose and Limitations

It has been a guiding principle throughout the work leading up to this thesis to derive all necessary equation in an as rigorous manner as possible and to document the results clearly. It is the hope of the author that these efforts will contribute to a deeper understanding about the strengths and weaknesses that the tools covered in this work possess. It should also be noted that the majority of tools used in this work are applicable to a much wider range of problems than Turbomachinery tonal noise, and consequently the results reported will hopefully be of use to a wider community than those specializing in Turbomachinery Computational Aeroacoustics.

2 Modeling Unsteady Turbomachinery Flows: The Harmonic Balance Method

A description of the flow field within a turbomachine can be obtained by numerically solving some formulation of the Navier-Stokes equations. Indeed, both the numerical method and mathematical form of the governing equations have a strong impact on the accuracy and detail that the solution provides. The most common formulation in use today for modeling unsteady, compressible flows in turbomachines is the Favre-Averaged Navier-Stokes equations coupled with some suitable eddy-viscosity turbulence model. These equations describe the spatial and temporal evolution of large scale fluid flow structures, and consequently require discretization in both space and time in order to be solved numerically. For spatial discretization, the Finite-Volume Method method available in the Chalmers-developed G3D::Flow solver framework has been used. Details on the spatial discretization and numerical schemes used in G3D::Flow can be found in [11, 12]. Temporal discretization is achieved with the Harmonic Balance method proposed by Hall et al. [13], which was added to G3D::Flow as a part of this thesis work. In this section the Harmonic Balance method is derived and some important properties of the technique are furthermore highlighted.

The derivation starts from the Favre-Averaged Navier-Stokes equations written in compact, conservative form as

$$\frac{\partial \mathcal{Q}}{\partial t} + \frac{\partial \mathcal{F}_j}{\partial x_j} = \mathcal{H} \tag{2.1}$$

Here, $\mathcal{Q}$ is a vector that contains the primary solution variables, also known as the conserved variables. For the Favre-Averaged Navier-Stokes equations they represent density, momentum, total energy and additional turbulence properties inherent to the type of turbulence model being used. The two remaining terms, $\mathcal{F}_j$ and $\mathcal{H}$, respectively contain the total (convective + viscous) flux of each conserved variable and possible source terms. The Harmonic Balance method is applicable when the solution is known to be periodic in time. In these cases, the conserved variables in Eq. (2.1) can be expressed as a Fourier series in time, with spatially varying Fourier coefficients

$$\mathcal{Q}(t, \mathbf{x}) = \sum_{n=-\infty}^{\infty} \hat{\mathcal{Q}}_n(\mathbf{x}) e^{i\omega_n t} \tag{2.2}$$

This equation shows that a periodic solution can be represented by an infinite series of harmonics, with frequencies that are integer multiples of the fundamental frequency: $\omega_n = 2\pi n/T$. For a CROR, the solution in the relative frame of reference attached to either of the counter rotating blade rows will be periodic with a fundamental frequency equal to the relative blade passing frequency of the adjacent blade row. If the effects of an upstream pylon or angle of attack of the CROR would be included in the simulation additional fundamental frequencies will also appear. For such purposes a more general formulation of the the Harmonic Balance method must be applied, see e.g. [14, 15, 16]. In this work only an isolated CROR at zero angle of attack has been considered and

the original form of the Harmonic Balance method is therefore applicable without any modifications. The derivation is now continued by assuming that a limited number of the harmonics in Eq. (2.2) are sufficient to accurately describe the solution, and the effects of the higher ones are consequently discarded. Equation (2.2) can therefore be truncated as follows

$$\mathcal{Q}(t) \approx \sum_{n=-N_h}^{N_h} \hat{\mathcal{Q}}_n e^{i\omega_n t} \tag{2.3}$$

Here, N_h represents the highest harmonic that is included in the solution. This approximation can now be combined with the Nyquist sampling theorem, which states that a solution containing at most N_h harmonics is uniquely determined from its values at $N_t = 2N_h + 1$ samples equally distributed over the time period [17]. A new solution vector $\mathcal{Q}^*$ that contains this sampling is therefore introduced as follows

$$\mathcal{Q}^* = [\ \mathcal{Q}_0,\ \mathcal{Q}_1,\ \dots\ ,\ \mathcal{Q}_{N_t-1}\ ]^T \tag{2.4}$$

In this expression, $\mathcal{Q}_l = \mathcal{Q}(t_l)$, where $t_l = lT/N_t$ is the time at time level l . Given $\mathcal{Q}^*$, the complete solution is obtained by calculating the Fourier coefficients in Eq. (2.3) using a discrete Fourier transform as follows

$$\hat{\mathcal{Q}}_n = \frac{1}{N_t} \sum_{l=0}^{N_t-1} \mathcal{Q}_l\ e^{-i\omega_n t_l} \tag{2.5}$$

In the Harmonic Balance method, the preceding argument and assumptions are used to rewrite Eq. (2.1) into an equation for $\mathcal{Q}^*$ as follows. First, Eq. (2.3) is differentiated with respect to time and combined with Eq. (2.5) to obtain

$$\frac{\partial \mathcal{Q}}{\partial t} \approx \sum_{n=-N_h}^{N_h} i\omega_n \left(\frac{1}{N_t} \sum_{l=0}^{N_t-1} \mathcal{Q}_l\ e^{-i\omega_n t_l} \right) e^{i\omega_n t} \tag{2.6}$$

By interchanging the order of summation, combining the exponential terms and evaluating the resulting expression at time level m the following is obtained

$$\frac{\partial \mathcal{Q}_m}{\partial t} \approx \sum_{l=0}^{N_t-1} \left(\frac{i}{N_t} \sum_{n=-N_h}^{N_h} \omega_n e^{i\omega_n (t_m - t_l)} \right) \mathcal{Q}_l \tag{2.7}$$

This equation expresses the time derivative at time level m as a finite difference taken over all other time levels. This can also be written in matrix notation as follows

$$\frac{\partial \mathcal{Q}^*}{\partial t} \approx D\mathcal{Q}^* \tag{2.8}$$

Here, D is known as the time spectral derivative matrix and is block structured into $N_t \times N_t$ blocks. Each block contains a diagonal matrix of size $N_{var} \times N_{var}$, where N_{var} is the number of conserved variables present in $\mathcal{Q}$. The entries of the diagonal matrix in block (m, l) are all equal and will here be denoted $d_{m,l}$. A compact analytical expression

for these elements may be obtained by evaluating the summation within the parenthesis of Eq. (2.7), for a complete derivation see [18]

$$d_{m,l} = \begin{cases} 0 & l = m \\ \frac{\pi}{T}(-1)^{(m-l)} \csc\left(\frac{\pi(m-l)}{N_t}\right) & l \neq m \end{cases} \tag{2.9}$$

The final step in the construction of a governing equation for $\mathcal{Q}^*$ is to require that the time derivative, as calculated from Eq. (2.8), balances the flux and source terms at each time level. This gives the following final equation

$$D\mathcal{Q}^* + \frac{\partial \mathcal{F}_j^*}{\partial x_j} = \mathcal{H}^* \tag{2.10}$$

Here, $\mathcal{F}_j^*$ and $\mathcal{H}^*$ respectively contain the total flux and source terms at each individual time level. Eq. (2.10) represents a coupled set of mathematically steady state equations for the samples of the solution at the N_t time levels.

2.1 Properties of the Harmonic Balance Solution

2.1.1 Modal Decomposition

The time spectral derivative defined in Eq. (2.8) may be applied to a single conserved variable at a time due to the block structure of D. In this case the time spectral derivative operation becomes a matrix vector multiplication between a $N_t \times N_t$ matrix $\tilde{D}$ and a vector q^p that contains the p^{th} conserved variable at all time levels. The matrix $\tilde{D}$, whose elements $\tilde{d}_{m,l}$ are given by Eq (2.9), turns out to have N_t unique eigenvalues ξ_n whose corresponding eigenvectors $\hat{h}_n$ are orthogonal. These eigenvalue/eigenvector pairs are given by the following formula

$$\xi_n = i\omega_n, \quad \hat{h}_n = \begin{bmatrix} e^{i\omega_n t_0} \\ e^{i\omega_n t_1} \\ \vdots \\ e^{i\omega_n t_{N_t-1}} \end{bmatrix}, \quad n = -N_h, ..., 0, ..., N_h \tag{2.11}$$

From this equation it can be seen that the eigenvalues correspond to the frequencies included in the Harmonic Balance computation times the imaginary unit. The corresponding eigenvectors are in addition obtained by evaluating the harmonic for each of these frequencies at all N_t time levels. It is also interesting to note that the time spectral derivative matrix correctly measures the time derivative of each harmonic since $\tilde{D}\hat{h}_n = \xi_n \hat{h}_n = i\omega_n \hat{h}_n$ indeed is the time derivative of the harmonic evaluated at all N_t time levels

A set of N_t orthogonal vectors form a basis for $\mathbb{R}^{N_t}$ (or $\mathbb{C}^{N_t}$) [19]. This implies that any $q^p \in \mathbb{R}^{N_t}$ can be uniquely represented by a linear combination of the eigenvectors to

$\tilde{D}$ as follows

$$q^p = \sum_{n=-N_h}^{N_h} \hat{q}_n^p \hat{h}_n \tag{2.12}$$

The scalar weights in Eq. (2.12) are obtained from the orthogonal projection of q^p onto $\hat{h}_n$ according to [19]

$$\hat{q}_n^p = \frac{1}{\langle \hat{h}_n | \hat{h}_n \rangle} \langle q^p | \hat{h}_n \rangle \tag{2.13}$$

Here, $\langle \cdot | \cdot \rangle$ is the inner product on $\mathbb{C}^{N_t}$ which is defined in the same way as the the normal Euclidean inner product except that the second element is the complex conjugate. Note that since $\langle \hat{h}_n | \hat{h}_n \rangle = N_t$, Eq. (2.12) and (2.13) respectively correspond to Eq. (2.3) and (2.5) applied to a single conserved variable.

The modal decomposition defined in this section will be used next to demonstrate the concept of aliasing. After this, the eigenvalues of a different type of matrix operator known as the time spectral viscosity operator will be analyzed in order to draw conclusions on its properties. A very good demonstration of how the eigenvalues of an operator affects is properties is provided in [20]. It should also be noted that this reference performs an analogous modal decomposition to the one presented here, but for spatially periodic problems, in order to derive some important properties of spatial discretization schemes.

2.1.2 Aliasing

The concept of aliasing may be summarized by the following statement

Aliasing. *Suppose that a Harmonic Balance solution $q^p \in \mathbb{R}^{N_t}$ has been generated by a set of known Fourier coefficients $\hat{q}_n^p$ using Eq.* (2.12)*. Further suppose that a new solution $\tilde{q}^p$ is constructed by adding a harmonic with frequency ω_k, $|k| > N_h$, and amplitude $\hat{q}_k^p$ to q^p according to*

$$\tilde{q}^p = q^p + \hat{q}_k^p \hat{h}_k \tag{2.14}$$

Then the same Fourier coefficients used to generate q^p can not be obtained by inserting $\tilde{q}^p$ into Eq. (2.13)*. The difference is caused by the amplitude of the higher frequency harmonic, meaning that it has become a low frequency alias.*

Proof. In order to prove the above statement a two step approach is used. First, it is shown that the value of $\hat{q}_k^p$ can not be determined uniquely from $\tilde{q}^p$. This gives that q^p can not be obtained from $\tilde{q}^p$ by inverting Eq. (2.14). The second step of the proof is to show that q^p and $\tilde{q}^p$ yield different Fourier coefficients when inserted into Eq. (2.13) and that the difference indeed is due to the presence of $\hat{q}_k^p$.

The first part of the proof can be proven by means of contradiction. Assume therefore that all $N_h + 2$ unknown Fourier coefficients can be determined uniquely. This implies

that the following matrix equation has a unique solution

$$\tilde{q}^p = \underbrace{\left[\hat{h}_{-N_h}, \hat{h}_{-N_h+1}, \cdots, \hat{h}_{N_h}, \hat{h}_k\right]}_{A} \underbrace{\left[\hat{q}^p_{-N_h}, \hat{q}^p_{-N_h+1}, \cdots, \hat{q}^p_{N_h}, \hat{q}^p_k\right]^T}_{\mathbf{x}} \tag{2.15}$$

The matrix A is of size $N_t \times N_t + 1$ and satisfies $rank(A) = N_t$ since the first N_t columns are orthogonal. From this observation it follows that one solution to Eq. (2.15) can be obtained by computing the orthogonal projection of $\tilde{q}^p$ onto the first N_t columns in A according to

$$\mathbf{x}_p = \frac{1}{N_t} \begin{bmatrix} \langle \tilde{q}^p | \hat{h}_{-N_h} \rangle \\ \langle \tilde{q}^p | \hat{h}_{-N_h+1} \rangle \\ \vdots \\ \langle \tilde{q}^p | \hat{h}_{N_h} \rangle \\ 0 \end{bmatrix} \tag{2.16}$$

Now for any $\alpha \in \mathbb{C}$ construct a vector $\mathbf{x}_h$ as follows

$$\mathbf{x}_h = \frac{\alpha}{N_t} \begin{bmatrix} -\langle \hat{h}_k | \hat{h}_{-N_h} \rangle \\ -\langle \hat{h}_k | \hat{h}_{-N_h+1} \rangle \\ \vdots \\ -\langle \hat{h}_k | \hat{h}_{N_h} \rangle \\ N_t \end{bmatrix} \tag{2.17}$$

This vector satisfies $A\mathbf{x}_h = 0$, coming from the fact that $\hat{h}_k \in \mathbb{C}^{N_t}$ and therefore can be expressed as a linear combination of the eigenvector to $\tilde{D}$. But then the vector $\mathbf{x}_p + \mathbf{x}_h$ is also a solution to Eq. (2.15), which contradicts the original assumption.

In order to complete the proof it must now be proven that the Fourier coefficients obtained by inserting either q^p or $\tilde{q}^p$ into Eq. (2.13) gives different results and that the difference is due to $\hat{q}^p_k$. In order to do this, note that for the particular case when $\alpha = \hat{q}^p_k$ one obtains

$$\mathbf{x}_p + \mathbf{x}_h = \begin{bmatrix} \hat{q}^p_{-N_h} \\ \hat{q}^p_{-N_h+1} \\ \vdots \\ \hat{q}^p_{N_h} \\ \hat{q}^p_k \end{bmatrix} \tag{2.18}$$

This is in fact the solution of Eq. (2.15) that contains the correct Fourier coefficients used to generate $\tilde{q}^p$ in the first place. Also note that the first N_t elements of the vectors $\mathbf{x}_p$ and $\mathbf{x}_p + \mathbf{x}_h$ respectively contains the Fourier coefficients obtained by inserting $\tilde{q}^p$ and q^p into Eq. (2.13). Since the vector $\mathbf{x}_h$ is non-zero for any nonzero $\hat{q}^p_k$, it follows that the Fourier coefficients indeed are different and that the difference has been introduced by the higher harmonic. This completes the proof. □

The implication of the above statement is that if a higher frequency harmonic finds its way into a Harmonic Balance solution it can not be eliminated. Instead, it will change the amplitude (energy) of the lower frequency harmonics which results in that the time derivative of the these harmonics are wrongly measured by D which could result in bad convergence or poor results. For this reason it is important to formulate the boundary conditions in such a way that they only add resolved frequencies to the solution. This is however not always enough since higher frequency harmonics also can be generated when solution is being computed. This can be seen from the fact that the flux and source terms in Eq. (2.10) are nonlinear functions of the solution variables [16]. Thus, when the residual, which is used to update the solution from one iteration to the next, is being computed from the flux and source terms, higher frequency harmonics will be generated and added to the solution. This problem naturally becomes more severe for strongly nonlinear problems.

2.1.3 Modal Damping using Time Spectral Viscosity

The eigenvalues of the time spectral derivative matrix derived in section 2.1.1 were found to be purely imaginary. This implies that no damping is added to the temporal modes (eigenvectors) as the solution is being computed. Although this is a desirable feature, there may be situations when adding some artificial damping to the modes may be necessary. One such case, which was mentioned in the previous section, is when frequencies that are generated by the nonlinear terms in Eq. (2.10) are not included in the Harmonic Balance computation. Indeed, if all frequencies would be included, the higher frequencies will eventually be dissipated by either physical or numerical mechanisms. When these "natural" dissipation mechanisms are no longer present, the energy of the higher frequency harmonics will instead be added to the lower harmonics through aliasing. In these cases it would be natural to include an additional term in Eq. (2.10) that adds some artificial damping to the lower frequency harmonics in order to dissipate the energy added to them by aliasing.

One approach for introducing modal damping is the time spectral viscosity operator proposed by Huang and Ekici [21]. This operator introduces a damping which is proportional to the second derivative in time of the selected modes. It can be obtained similarly to how the time spectral derivative was derived, with the main difference that the Fourier series is differentiated twice with respect to time and only harmonics that should be damped are kept in the series expansion. This results in a new matrix operator V with the same structure as D in which the diagonal elements of block (m, l) are given by

$$v_{m,l} = -\frac{2}{N_t} \sum_{n \in \mathcal{V}} \varepsilon_n \omega_n^2 \cos\left(\frac{2\pi n(m-l)}{N_t}\right) \tag{2.19}$$

Here, $\mathcal{V}$ represents the set of modes (both the positive and negative indices) that should be damped, e.g. $\{\{1,-1\},\{2,-2\}\}$. The parameter $\varepsilon_n > 0$ is the viscosity coefficient/damping amplitude which should be the same for each positive and negative index pair. The fact that the time spectral viscosity operator will act as a damping term can be seen from that the modes $\hat{h}_n$, $n \in \mathcal{V}$, are eigenvectors to V with corresponding negative,

real eigenvalues $-\varepsilon_n\omega_n^2$ whereas the remaining modes have eigenvalue 0. Therefore, when the time spectral viscosity operator is added to the right hand side of Eq. (2.10) it will indeed damp the selected modes, with a damping that is proportional to $\varepsilon_n\omega_n^2$.

In some sense, the time spectral viscosity operator is similar to the eddy viscosity approach used in RANS/LES turbulence modeling although it uses a very simple closure model (constant) for the viscosity coefficient. It is plausible that it would be possible to derive a more sophisticated closure model for ε_n in order to keep the lower frequency harmonics alias free, although this has not been attempted in this thesis. Instead the time spectral viscosity operator was used in Paper B to damp out the unsteady harmonics of the turbulent properties in order to stabilize the computations.

2.2 Stability Analysis of the Harmonic Balance Method

In order to solve the Harmonic Balance equations presented in Eq. (2.10) a pseudo time derivative is added to them as follows

$$\frac{\partial \mathcal{Q}^*}{\partial \tau} + D\mathcal{Q}^* + \frac{\partial \mathcal{F}_j^*}{\partial x_j} = \mathcal{H}^* \tag{2.20}$$

After Eq. (2.20) has been discretized in space the explicit three stage Runge-Kutta method available in G3D::Flow for time accurate simulations is used to advance the equations in pseudo time using local time stepping. The motivation for doing this is that if a steady state is reached, meaning that $\frac{\partial \mathcal{Q}^*}{\partial \tau} = 0$, then a solution to Eq. (2.10) has been obtained. In order to accelerate convergence towards a steady state the pseudo time step is adjusted to be as large as possible in every cell of the computational mesh, without violating the stability limits of the numerical scheme. For hyperbolic conservation laws, such as the Navier-Stokes equations, the upper limit on the time step is governed by the largest Courant-Friedrichs-Lewy (CFL) number that the numerical scheme allows. In addition to this, the time spectral derivative found in the Harmonic Balance equations has been shown to put additional constraints on the size of the time step [22, 23]. From this argument it is thus apparent that knowledge about the stability limits of the numerical method is vital for obtaining converged results in the least amount of iterations possible. For this purpose, the stability limit of the numerical method used in G3D::Flow to solve Eq. (2.20) will be derived in this section by using the Von Neumann method [24, 20]. The derivation is closely related to the work by Gentilli [22], with the main difference that a different dimensionless parameters is chosen in the end to define the stability limits of the solver.

2.2.1 Derivation of Governing Equations on Characteristic Form

Before the stability analysis is performed Eq. (2.20) will be rewritten in a simpler form. To begin with, it is assumed that the problem is one dimensional in space and that viscous effects are negligible. This reduces the Eq. (2.20) to the Harmonic Balance form of the

one dimensional Euler equations

$$\frac{\partial \mathcal{Q}^*}{\partial \tau} + D\mathcal{Q}^* + \frac{\partial \mathcal{F}^*}{\partial x} = 0 \tag{2.21}$$

Note that in this equation, $\mathcal{Q}^*$ only contains density, momentum and total energy and $\mathcal{F}^*$ is now the convective flux vector. Equation (2.21) can be expressed in quasi linear form by using the chain rule to rewrite the gradient of the flux vector as follows

$$\frac{\partial \mathcal{Q}^*}{\partial \tau} + D\mathcal{Q}^* + \frac{\partial \mathcal{F}^*}{\partial \mathcal{Q}^*}\frac{\partial \mathcal{Q}^*}{\partial x} = 0 \tag{2.22}$$

In this equation $\frac{\partial \mathcal{F}^*}{\partial \mathcal{Q}^*}$ is known as the flux Jacobian matrix and it is structured into $N_t \times N_t$ blocks, each of size $N_{var} \times N_{var}$. Only the diagonal blocks of this matrix are non-zero and they respectively contain the flux Jacobian of the Euler equations evaluated at each of the N_t time levels used in the Harmonic Balance computation. For the purpose of the stability analysis it will however be assumed that the flux Jacobian matrix is constant and obtained from the mean flow state. This reduces the problem to being linear in the conserved variables. Before the Von Neumann method can be used Eq. (2.21) must also be uncoupled with respect to the solution variables. This is achieved by introducing the diagonalization of the flux Jacobian defined as follows

$$\frac{\partial \mathcal{F}^*}{\partial \mathcal{Q}^*} = T^* \Lambda^* T^{*-1} \tag{2.23}$$

Here, T^* and Λ^* both have the same block structure as the flux Jacobian and the diagonal blocks of these matrices respectively contain the eigenvectors and eigenvalues for the flux Jacobian of the Euler equations. For the one dimensional case considered here, the eigenvalues are U_0, $U_0 + c_0$ and $U_0 - c_0$, where U_0 and c_0 are the mean velocity and speed of sound respectively. By inserting Eq. (2.23) into (2.21) a new differential equation for the characteristic variables $\mathcal{W}^*$ may be derived as

$$\frac{\partial \mathcal{W}^*}{\partial \tau} + D\mathcal{W}^* + \Lambda^* \frac{\partial \mathcal{W}^*}{\partial x} = 0 \tag{2.24}$$

To obtain this equation the fact that the eigenvector matrix T^* commutes with D has been used together with the definition of the characteristic variables which reads

$$\mathcal{W}^* = T^{*-1}\mathcal{Q}^* \tag{2.25}$$

The important property of Eq. (2.24) is that it represents a set of uncoupled transport equations for the characteristic variables, each propagating with its own characteristic speed given by the corresponding eigenvalue of the flux Jacobian. Thus, if w_l^p denotes the value of the p^{th} characteristic variable at time level l and λ_p denotes the corresponding characteristic speed, then Eq. (2.24) may be written as

$$\frac{\partial w_l^p}{\partial \tau} + \sum_{t=0}^{N_t-1} d_{l,t} w_t^p + \lambda_p \frac{\partial w_l^p}{\partial x} = 0 \tag{2.26}$$

Note that there is no summation with respect to p in the last term on the left hand side. Although Eq. (2.26) looks vastly different from Eq. (2.20), the new equation is actually very relevant for the purpose of analyzing the stability of the discretization schemes used in compressible CFD codes. This is because upwind biased discretization schemes, which are commonly used to discretize the flux term, are dependent on knowledge of the proper direction of propagation of information, i.e. the characteristic speeds λ_p, in order to be stable [20]. This is indeed the case for the upwind scheme used in G3D::Flow, which splits the flux vector according to the above recipe in order to calculate convective fluxes. Now that a linear set of equations for each characteristic variable has been obtained one may proceed to analyze the stability of the discretized form by means of the Von Neumann method.

2.2.2 Stability of Numerical Discretization

A standard Von Neumann stability analysis considers the (pseudo-) time evolution of a numerical solution that is periodic in space [24, 20]. If the spatial periodicity is denoted $2L$ and it is assumed that $2N$ cells exactly fit into this period then the computational mesh will look as illustrated in figure 2.1. Note that in this figure, all N_t time levels used for the temporal discretization have also been included. The spatial and temporal periodicity assumptions implies that the numerical solution of w_l^p at pseudo time instant m and grid node k can be written as

$$w_l^p|_k^m = \sum_{n=-N_h}^{N_h} \sum_{j=-N}^{N} \hat{u}_{n,j}^m e^{i\omega_n t_l} e^{ik_j x_k} \tag{2.27}$$

Here, the angular frequency and spatial wavenumber are defined as

$$\begin{aligned} \omega_n &= \frac{2\pi n}{T} \\ k_j &= \frac{2\pi j}{2L} \end{aligned} \tag{2.28}$$

The exponents in Eq. (2.27) may be rewritten by using the definition of the physical time t_l the axial position x_k according to

$$\begin{aligned} \omega_n t_l &= \frac{2\pi n}{T}\frac{lT}{N_t} = \frac{2\pi n}{N_t} l = \psi l \\ k_j x_k &= \frac{2\pi j}{2L}\frac{kL}{N} = \frac{\pi j}{N} k = \phi k \end{aligned} \tag{2.29}$$

The new variables ψ and ϕ defined in Eq. (2.29) may take on any values between $-\pi$ and π since N_h and N can be chosen arbitrarily dependent on the numerical setup of a particular problem. These new variables respectively denote the angular frequency and wave number of a particular mode in relation to the highest frequency/wavenumber that can be resoled by the computational mesh. Values close to zero implies that the wavelength is much larger than the grid spacing whereas values close to $\pm\pi$ means that the wavelength is close to the Nyquist limit.

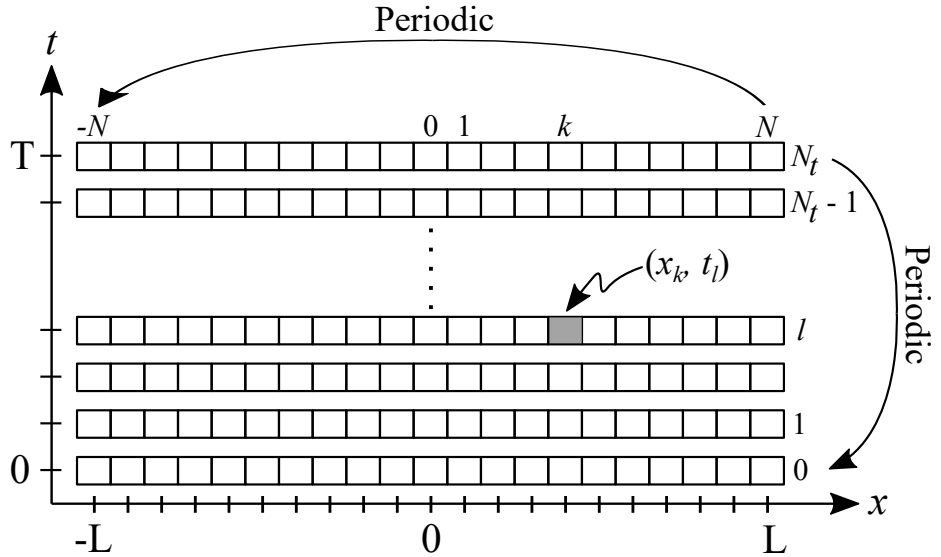

Figure 2.1: *Schematic View of the Discretization used for Stability Analysis of the Harmonic Balance Method.*

The linear nature of Eq. (2.26) implies that all modes in Eq. (2.27) will develop independently of each other as the solver advances in pseudo time. It is thus sufficient to study the evolution of a single mode at a time in order to draw conclusions on the stability of the numerical scheme. For this purpose the following shorthand notation for a single mode in Eq. (2.27) is introduced

$$\begin{aligned} u^m_{l,k}(\psi,\phi) &= \hat{u}^m_{n,j} e^{i\omega_n t_l} e^{ik_j x_k} \\ &= \hat{u}^m(\psi,\phi) e^{i\psi l} e^{i\phi k} \end{aligned} \tag{2.30}$$

By substituting this single mode into Eq. (2.26) and integrating the resulting expression over the k^{th} cell the following is obtained

$$\Delta x \frac{\partial u^m_{l,k}}{\partial \tau} + \Delta x \sum_{t=0}^{N_t-1} d_{l,t} u^m_{t,k} + \lambda \left(u^m_{l,k+\frac{1}{2}} - u^m_{l,k-\frac{1}{2}} \right) = 0 \tag{2.31}$$

Here, $\Delta x = L/N$ is the width of the cell and $k \pm \frac{1}{2}$ is used to indicate that the quantity is evaluated at the right/left cell face. The time spectral derivative term can be rewritten by utilizing the results of section 2.1.1 to obtain the following

$$\Delta x \frac{\partial u^m_{l,k}}{\partial \tau} + \Delta x \frac{i\psi N_t}{T} u^m_{l,k} + \lambda \left(u^m_{l,k+\frac{1}{2}} - u^m_{l,k-\frac{1}{2}} \right) = 0 \tag{2.32}$$

In G3D::Flow, two cells on each side of a call face are used to calculate a face value. The upstream cell values, defined based on the sign of λ, are are slightly biased in order to generate some artificial dissipation compared to using a completely symmetric (central)

weighting. The amount of bias is defined by blending the central weighting, which is fourth order accurate, with a third order accurate upwind biased weighting that uses two upstream and one downstream value. This results in a formally third order accurate flux scheme with variable amount of artificial dissipation. More details on the flux schemes used in G3D::Flow can be found in [11]. If the net flux calculated by the scheme is denoted F then Eq. (2.32) may be written as

$$\frac{\partial u_{l,k}^m}{\partial \tau} + \frac{i\psi N_t}{T} u_{l,k}^m + \frac{\lambda}{\Delta x} F(u_{l,k-2}^m, ..., u_{l,k+2}^m) = 0 \tag{2.33}$$

The three stage Runge-Kutta method implemented in G3D::Flow can now be used to discretize the pseudo time derivative and obtain a relation for $u_{l,k}^{m+1}$ as a function of the cell values $\cdots, u_{l,k-1}^m, u_{l,k}^m, u_{l,k+1}^m, \cdots$. From this relation an expression for the ratio $\hat{u}^{m+1}/\hat{u}^m$ can then be derived since the exponential terms defined in Eq. (2.30) will cancel. This ratio is the fundamental ingredient of the Von Neumann method since it describes the evolution of each mode between two subsequent (pseudo-) time steps. For the Harmonic Balance method it turns out to become a function of the following parameters

$$\frac{\hat{u}^{m+1}}{\hat{u}^m} = G\left(\phi, \frac{\lambda \Delta\tau}{\Delta x}, \frac{\psi N_t \Delta\tau}{T}\right) \tag{2.34}$$

The second parameter in this expression is the well known CFL number that stems from the discretization of the convective flux term in Eq. (2.26). The third parameter has on the other hand been introduced by the Harmonic Balance method and can be seen to be proportional to the ratio $\Delta\tau/(T/N_t)$. This ratio can for convenience also be expressed as the ratio between the CFL number and a new parameter that here will be defined as the Harmonic Balance CFL number

$$CFL_{HB} = \frac{\lambda T/N_t}{\Delta x} \tag{2.35}$$

With this definition a new functional form of Eq. (2.34) may be obtained as follows

$$\frac{\hat{u}^{m+1}}{\hat{u}^m} = G\left(\phi, CFL, \psi, CFL_{HB}\right) \tag{2.36}$$

The Von Neumann stability criteria may now be stated as follows: For a specific combination of CFL and CFL_{HB} numbers it must hold that [24, 20]

$$|G| \leq 1, \quad \forall \phi, \psi \in (-\pi, \pi) \tag{2.37}$$

For convenience the function G was calculated analytically using the symbolic function features available in the MATLAB$^{\text{TM}}$ software. The stability criteria in Eq. (2.37) was then evaluated for a range of CFL number pairs in order to generate a line in the (CFL, CFL_{HB}) plane that separates the stable from the unstable region. The result of this computation is demonstrated in figure 2.2 for two convective flux schemes. The trend demonstrated in this figure is clear, when the Harmonic Balance CFL number decreases, which corresponds to either high frequencies (low T) or a large amount of time levels

(high N_t), the limiting CFL number that ensures stability decreases as well. Thus, the pseudo time step is now a function not only of the spatial grid spacing but indeed also of the temporal grid spacing.

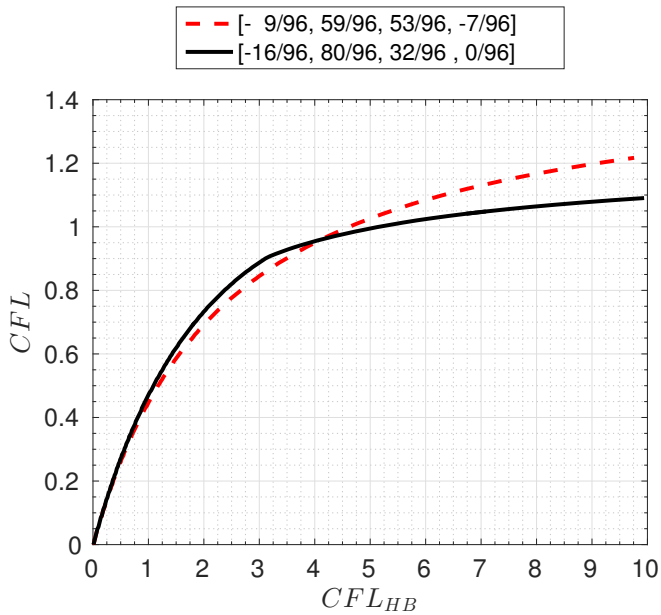

Figure 2.2: *Stability region in (CFL, CFL_{HB}) plane for the explicit Harmonic Balance solver used in G3D::Flow. Area below/to the right of the lines represents the stable region. Results are demonstrated for two different set of weights used to calculate the face value in the convective flux scheme.*

The theoretical stability boundary presented in figure 2.2 has also been investigated numerically by computing the propagation of a periodic Gaussian pulse in one dimension with the Harmonic Balance method for different combinations of CFL and CFL_{HB} numbers. The Gaussian pulse was chosen as the model problem since its Fourier transform also have a Gaussian shape. This makes it easy to set the initial shape of the pulse such that all wavenumbers resolved on the computational grid have a significant amplitude and consequently that the stability condition in Eq. (2.37) can be checked by the computation. The limiting values of CFL and CFL_{HB} obtained from the numerical solutions were found to be very close to those predicted in figure 2.2 for both convective schemes. The discrepancies found were in the order of a few percent and can probably be attributed to that some unstable modes grew very slowly, thus making them hard to detect unless a very large amount of iterations are performed.

3 Generation and Propagation of Sound: The Acoustic Analogy

The aero-acoustic analogy was introduced by Sir Michael James Lighthill in order to define the processes through which noise is generated in a turbulent flow field [7, 8]. In his acoustic analogy an aerodynamic noise source is defined as the difference obtained from comparing the exact wave equation describing density perturbations in the fluid to the wave equation that governs acoustic propagation in the far field (where the flow is supposed to be uniform and at rest). The exact wave equation is obtained by rewriting the continuity and momentum equations which read

$$\begin{aligned} \frac{\partial \rho}{\partial t} + \frac{\partial \rho u_i}{\partial x_i} &= 0 \\ \frac{\partial \rho u_i}{\partial t} + \frac{\partial \rho u_i u_j}{\partial x_j} + \frac{\partial p_{ij}}{\partial x_j} &= 0 \end{aligned} \tag{3.1}$$

Here, $p_{ij} = p\delta_{ij} - \sigma_{ij}$ is the compressive stress tensor. By taking the time derivative of the continuity equation and then subtracting the divergence of the momentum equation from the resulting expression, the following equation may be obtained

$$\frac{\partial^2 \rho}{\partial t^2} = \frac{\partial^2 \rho u_i u_j}{\partial x_i \partial x_j} + \frac{\partial^2 p_{ij}}{\partial x_i \partial x_j} \tag{3.2}$$

Perturbation variables are now defined to be the difference between the local fluid state and the far field state as

$$\begin{aligned} \rho' &= \rho - \rho_0 \\ p' &= p - p_0 \\ u_i' &= u_i - U_{i,0} \end{aligned} \tag{3.3}$$

By introducing these perturbation variables into Eq. (3.2) and then subtracting $c_0^2 \frac{\partial^2 \rho'}{\partial x_i x_i}$ from both sides of the resulting expression the famous Lighthill equation is obtained as

$$\frac{\partial^2 \rho'}{\partial t^2} - c_0^2 \frac{\partial^2 \rho'}{\partial x_i \partial x_i} = \frac{\partial^2 T_{ij}}{\partial x_i \partial x_j} \tag{3.4}$$

This equation is seen to take on the form of an inhomogeneous wave equation. By comparing it to the ordinary wave equation it can be seen that the noise generation stems from spatial derivatives of the tensor T_{ij}, which often is referred to as the Lighthill tensor

$$T_{ij} = \rho u_i' u_j' + (p' - c_0^2 \rho')\delta_{ij} - \sigma_{ij} \tag{3.5}$$

Note that this equation was obtained from the assumption that the far field state is at rest, i.e. $U_{i,0} = 0$. The Lighthill equation presented in Eq. (3.4) can be formally solved by forming a convolution between the right hand side of Eq. (3.4) and a free-space Green's function to the wave operator. This will give the density fluctuation at

the observer expressed as a volume integral over the subset of $\mathbb{R}^3$ where T_{ij} has non-negligible amplitude. It should be noted that this solution will be exact since that all noise generating mechanisms and effects that the non-uniform flow field has on noise propagation are absorbed into the Lighthill tensor [7]. By utilizing the relation $p' = c_0^2 \rho'$, which is assumed to be valid at the observer, the pressure signal can finally be obtained at the observer.

An important achievement obtained by Lighthill is the direct connection between the sound at an observer and the noise sources defined in Eq. (3.5). The exact value of the noise sources are however still an unknown that must be obtained by other means, such as from a CFD simulation. Lighthill's analogy is however seldom used to post-process CFD simulations because of the fact that it does not take solid surfaces into account. The presence of stationary, solid, surfaces was later added to Lighthill's analogy by Curle [25]. An even more general acoustic analogy for surfaces in arbitrary motion was later developed by Ffowcs Williams and Hawkings [9].

The fundamental problem that occurs when solid surfaces are present is that the flow equations are no longer valid throughout $\mathbb{R}^3$, which prevents a free-space Green's function from being applied to solve Eq. (3.4). The pioneering idea introduced by Ffowcs Williams and Hawkings to solve this problem was to "cut out" the part of $\mathbb{R}^3$ where solid surfaces are present and replace this volume with a fluid attaining the far-field (observer) state. This approach is illustrated in figure 3.1, where the fluid in V is assumed to attain the state ρ_0, p_0 and $U_{i,0}$, whereas the fluid remains in its actual state outside of ∂V. If f is defined to be a scalar field such that $f(\mathbf{x}, t) < 0$ for $\mathbf{x} \in V$ and $f(\mathbf{x}, t) > 0$ elsewhere, new fluid fields defined throughout $\mathbb{R}^3$ may be defined in terms of the Heaviside step function as

$$\begin{aligned} \underline{\rho} &= \rho_0(1 - H(f)) + \rho H(f) \\ \underline{p} &= p_0(1 - H(f)) + pH(f) \\ \underline{u_i} &= U_{i,0}(1 - H(f)) + u_i H(f) \end{aligned} \tag{3.6}$$

At this point we note that the new fields satisfy Eq. (3.1) everywhere except at the boundary ∂V where they are discontinuous. This non-differentiability can be overcome by reinterpreting the new fields in terms of distributions, also known as generalized functions. In this thesis, only some basic results from generalized function theory will be used in order to derive the Ffowcs Williams-Hawkings equations. For a good introduction to the subject, including many useful formulas for aerodynamic and acoustic applications, the reader is referred to the work of Farassat [26]. Some more fundamentals on generalized function theory that also may help in following the derivation presented hereinafter may be found in introductory textbooks on the subjects of Fourier- and Functional analysis, see e.g. [17, 27]

Let $\mathcal{D}(\mathbb{R}^N)$ denote the set of all infinitely differentiable functions on $\mathbb{R}^N$ that have bounded support. A function $\phi(\mathbf{x})$ belonging to this set is commonly denoted a test function. From this a distribution $g[\phi] : \mathcal{D}(\mathbb{R}^N) \mapsto \mathbb{C}$ is defined as a continuous, linear mapping between the set of all test functions and the complex numbers. In other words, $g[\phi]$ is a continuous, linear functional defined on $\mathcal{D}(\mathbb{R}^N)$. For a rigorous definition of the concepts of linearity and continuity, see [27]. In case $g(\mathbf{x})$ is an integrable function, the

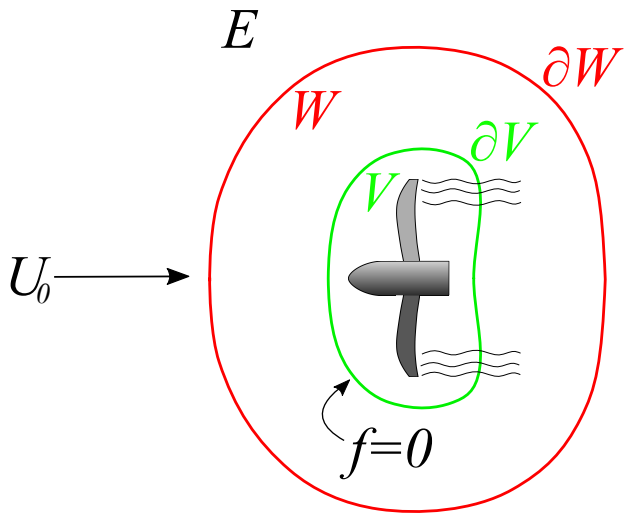

Figure 3.1: *Schematic View of the Ffowcs Williams-Hawkings Approach.*

corresponding distribution $g[\phi]$ is referred to as a regular distribution and the mapping is defined by an integral

$$g[\phi] = \int_{\mathbb{R}^N} g(\mathbf{x})\phi(\mathbf{x})d^N\mathbf{x} \tag{3.7}$$

This also defines the notation that will be used throughout this thesis, namely that the underlying function is denoted by g or $g(\mathbf{x})$, whereas the corresponding distribution is denoted $g[\phi]$. Note however that not all distributions can be defined in terms of an integral. These distributions are known as singular distributions [17]. The partial derivative of any distribution may be defined as follows [17]

$$\begin{aligned}(\partial^\alpha g)[\phi] &= (-1)^{|\alpha|} g[\partial^\alpha \phi] \\ \partial^\alpha &= \frac{\partial^{|\alpha|}}{\partial x_1^{\alpha_1} \partial x_2^{\alpha_2} \cdots \partial x_N^{\alpha_N}} \\ |\alpha| &= \alpha_1 + \alpha_2 + ... + \alpha_N\end{aligned} \tag{3.8}$$

for some positive integers $\alpha_1, ..., \alpha_N$. In the next section the continuity and momentum equations formulated in terms of distributional derivatives are derived. These are later combined in the same way as was done previously in order to derive the Lighthill equation. This will result in the famous Ffowcs Williams-Hawkings equation, which essentially is the Lighthill equation with some additional sources that account for the sound generation introduced by the discontinuity surface ∂V.

3.1 Derivation of the Convective Ffowcs Williams - Hawkings Equation

In the original paper by Ffowcs Williams and Hawkings an inhomogeneous wave equation for the special case when ∂V coincides with a solid surface is presented. The derivation presented in this paper does however not rely on this simplification and their theory is thus fully applicable to arbitrary surfaces that enclose all solid boundaries as shown in figure 3.1. A complete wave equation where the simplification was not included was later presented by Di Francescantonio [28]. In this latter case ∂V is often referred to as a porous surface, owing to the fact that fluid is allowed to cross it. The acoustic analogies cited so far all assumed that the surrounding fluid was at rest ($U_{i,0} = 0$). It is possible to include the effects of a uniform mean flow by moving both the observer and the surface when evaluating the integral solution of the inhomogeneous wave equation [29]. Another approach presented by Najafi-Yazidi et al. is to explicitly account for the presence of a uniform mean flow in the derivation [30]. The resulting wave equation, hereinafter referred to as the convective Ffowcs Williams-Hawkings equation, will include a convective wave operator, in which the time derivative is replaced by a Lagrangian derivative according to

$$\frac{\partial^2}{\partial t^2} - c_0^2 \frac{\partial^2}{\partial x_j \partial x_j} \rightarrow \left(\frac{\partial}{\partial t} + U_{j,0} \frac{\partial}{\partial x_j} \right)^2 - c_0^2 \frac{\partial^2}{\partial x_j \partial x_j} \tag{3.9}$$

In this thesis a derivation of the convective Ffowcs Williams-Hawkings equation for the case when ∂V is a stationary, porous surface is presented. The only simplification done is thus that the function f that defines ∂V only is a function of space, not time.

The derivation of the convective Ffowcs Williams-Hawkings equation starts with expressing the continuity and momentum equations in terms of derivatives of the distributions generated by the new fields defined in Eq. (3.6). By noting that the test functions are functions of both space and time the following is obtained

$$\begin{aligned}
\frac{\partial \rho}{\partial t}[\phi] + \frac{\partial \rho u_i}{\partial x_i}[\phi] &= -\int_t \int_{\mathbb{R}^3} \underline{\rho} \frac{\partial \phi}{\partial t} d^3\mathbf{x}dt - \int_t \int_{\mathbb{R}^3} \underline{\rho \underline{u}_i} \frac{\partial \phi}{\partial x_i} d^3\mathbf{x}dt \\
&= -\underbrace{\int_t \int_V \rho_0 \frac{\partial \phi}{\partial t} d^3\mathbf{x}dt}_{I} - \underbrace{\int_t \int_W \rho \frac{\partial \phi}{\partial t} d^3\mathbf{x}dt}_{II} \\
&\quad - \underbrace{\int_t \int_E \rho \frac{\partial \phi}{\partial t} d^3\mathbf{x}dt}_{III} - \underbrace{\int_t \int_V \rho_0 U_{i,0} \frac{\partial \phi}{\partial x_i} d^3\mathbf{x}dt}_{IV} \\
&\quad - \underbrace{\int_t \int_W \rho u_i \frac{\partial \phi}{\partial x_i} d^3\mathbf{x}dt}_{V} - \underbrace{\int_t \int_E \rho u_i \frac{\partial \phi}{\partial x_i} d^3\mathbf{x}dt}_{VI}
\end{aligned} \tag{3.10}$$

The terms I and II in Eq. (3.10) can be integrated by parts in time. Similarly the terms IV and V are integrated by parts using the divergence theorem. Since ϕ vanishes when

$t \to \pm\infty$ due to the bounded support of the test functions, the following is obtained

$$\begin{aligned}\frac{\partial \rho}{\partial t}[\phi] + \frac{\partial \rho u_i}{\partial x_i}[\phi] = &+ \underbrace{\int_t \int_V \frac{\partial \rho_0}{\partial t}\phi d^3\mathbf{x}dt}_{I} + \underbrace{\int_t \int_W \frac{\partial \rho}{\partial t}\phi d^3\mathbf{x}dt}_{II} \\ &- \underbrace{\int_t \int_E \rho \frac{\partial \phi}{\partial t} d^3\mathbf{x}dt}_{III} + \underbrace{\int_t \int_V \frac{\partial \rho_0 U_{i,0}}{\partial x_i}\phi d^3\mathbf{x}dt}_{IV} \\ &+ \underbrace{\int_t \int_W \frac{\partial \rho u_i}{\partial x_i}\phi d^3\mathbf{x}dt}_{V} - \underbrace{\int_t \int_E \rho u_i \frac{\partial \phi}{\partial x_i} d^3\mathbf{x}dt}_{VI} \\ &- \underbrace{\int_t \int_{\partial V} \rho_0 U_{i,0} n_i \phi dS dt}_{VII} + \underbrace{\int_t \int_{\partial V} \rho u_i n_i \phi dS dt}_{VIII} \\ &- \underbrace{\int_t \int_{\partial W} \rho u_i n_i \phi dS dt}_{IX}\end{aligned} \tag{3.11}$$

Here, dS is used to denote the area element of the surface that the integral is being evaluated over. Note that the integral denoted $VIII$ in Eq. (3.11) stems from the integration by parts of term V in Eq. (3.10) and that the sign of this integral has been changed in order to define the integral with a unit normal pointing out of the volume V. At this point it can noted that the combination of the terms I and IV in Eq. (3.11) will cancel since the mean flow satisfies the continuity equation inside V. The same argument results in that the terms II and V cancel. At this point the surface ∂W is allowed to go to infinity in the sense that it becomes large enough for ϕ to be zero on and outside it. This will make the terms III, VI and IX vanish, yielding the following final form of the continuity equation

$$\begin{aligned}\frac{\partial \rho}{\partial t}[\phi] + \frac{\partial \rho u_i}{\partial x_i}[\phi] &= \int_t \int_{\partial V} \left(\rho(U_{0,i} + u_i') - \rho_0 U_{i,0}\right) n_i \phi dS dt \\ &= Q[\phi]\end{aligned} \tag{3.12}$$

The integral on the right hand side now defines a new distribution $Q[\phi]$ that represents a mass flux term necessary for maintaining mass conservation on both sides of ∂V.

The momentum equation written in terms of derivatives of the distributions generated

by the fields in Eq. (3.6) is furthermore given by

$$\begin{aligned}\frac{\partial \rho u_i}{\partial t}[\phi] + \frac{\partial \rho u_i u_j}{\partial x_j}[\phi] + \frac{\partial p_{ij}}{\partial x_j}[\phi] = &- \underbrace{\int_t \int_V \rho_0 U_{i,0} \frac{\partial \phi}{\partial t} d^3\mathbf{x}dt}_{I} - \underbrace{\int_t \int_W \rho u_i \frac{\partial \phi}{\partial t} d^3\mathbf{x}dt}_{II} \\ &- \underbrace{\int_t \int_E \rho u_i \frac{\partial \phi}{\partial t} d^3\mathbf{x}dt}_{III} \\ &- \underbrace{\int_t \int_V (\rho_0 U_{i,0} U_{j,0} + p_0 \delta_{ij}) \frac{\partial \phi}{\partial x_j} d^3\mathbf{x}dt}_{IV} \\ &- \underbrace{\int_t \int_W (\rho u_i u_j + p_{ij}) \frac{\partial \phi}{\partial x_j} d^3\mathbf{x}dt}_{V} \\ &- \underbrace{\int_t \int_E (\rho u_i u_j + p_{ij}) \frac{\partial \phi}{\partial x_j} d^3\mathbf{x}dt}_{VI}\end{aligned} \tag{3.13}$$

In this equation the term IV has been simplified by the fact that the viscous stress tensor $\sigma_{ij} = 0$ inside the volume V. The procedure for rewriting the right hand side of Eq. (3.13) follows the same procedure as for the continuity equation. First, the terms I and II are integrated by parts in time and the fact that the test functions vanish at infinity is used to remove the integrated terms. The divergence theorem is then used to integrate the terms IV and V by parts. The volume integrals over V and W resulting from the integration by parts can then be canceled since the momentum equation is satisfied inside both these volumes. By then letting ∂W grow to infinity all integrals over ∂W and E will finally disappear to yield the following expression

$$\begin{aligned}\frac{\partial \rho u_i}{\partial t}[\phi] + \frac{\partial \rho u_i u_j}{\partial x_j}[\phi] + \frac{\partial p_{ij}}{\partial x_j}[\phi] &= \int_t \int_{\partial V} [\rho u_i u_j - \rho_0 U_{i,0} U_{j,0} + (p - p_0)\delta_{ij} - \sigma_{ij}] n_j \phi dS dt \\ &= \tilde{L}_i[\phi]\end{aligned} \tag{3.14}$$

The integral on the right hand side defines the distribution $\tilde{L}_i[\phi]$ which represents an extra momentum flux necessary to satisfy conservation of momentum on both sides of ∂V. In order to rigorously derive the convective Ffowcs Williams-Hawkings equations new discontinuous perturbation variables are now defined based on Eq. (3.6) as

$$\begin{aligned}\underline{\rho}' &= \underline{\rho} - \rho_0 \\ \underline{p}' &= \underline{p} - p_0 \\ \underline{u}_i' &= \underline{u}_i - U_{i,0}\end{aligned} \tag{3.15}$$

It is easy to verify that these definitions are equivalent to the perturbation variables defined in Eq. (3.3) multiplied by $H(f)$, e.g. $\underline{\rho}' = H(f)\rho'$. The distributions defined by

the discontinuous perturbation variables will be denoted by e.g. $\rho'[\phi]$ for the density. It is easy to verify that these new distributions satisfy the following intuitive relation

$$(\partial^\alpha \rho)[\phi] = (\partial^\alpha \rho')[\phi] \tag{3.16}$$

By taking the material derivative of the continuity equation (3.12) and subtracting the divergence of the momentum equation (3.14) the following is obtained

$$\begin{aligned}\frac{\partial^2 \rho}{\partial t^2}[\phi] + U_{j,0}\frac{\partial^2 \rho}{\partial x_j \partial t}[\phi] + U_{j,0}\frac{\partial^2 \rho u_i}{\partial x_j \partial x_i}[\phi] - \frac{\partial^2 \rho u_i u_j}{\partial x_i x_j}[\phi] = &\left(\frac{\partial}{\partial t} + U_{j,0}\frac{\partial}{\partial x_j}\right) Q[\phi] \\ &- \frac{\partial}{\partial x_i}\tilde{L}_i[\phi] \\ &+ \frac{\partial^2 p_{ij}}{\partial x_i \partial x_j}[\phi]\end{aligned} \tag{3.17}$$

The two last terms on the left hand side of Eq. (3.17) can be rewritten as follows using the continuity equation

$$\begin{aligned}U_{j,0}\frac{\partial^2 \rho u_i}{\partial x_j \partial x_i}[\phi] - \frac{\partial^2 \rho u_i u_j}{\partial x_i x_j}[\phi] &= + U_{i,0}U_{j,0}\frac{\partial^2 \rho}{\partial x_j \partial x_i}[\phi] + U_{j,0}\frac{\partial^2 \rho u_i'}{\partial x_j \partial x_i}[\phi] \\ &\quad - U_{j,0}\frac{\partial^2 \rho u_i}{\partial x_j \partial x_i}[\phi] - U_{i,0}\frac{\partial^2 \rho u_j'}{\partial x_i \partial x_j}[\phi] - \frac{\partial^2 \rho u_i' u_j'}{\partial x_i \partial x_j}[\phi] \\ &= + U_{i,0}U_{j,0}\frac{\partial^2 \rho}{\partial x_j \partial x_i}[\phi] - U_{j,0}\frac{\partial}{\partial x_j}Q[\phi] \\ &\quad + U_{j,0}\frac{\partial^2 \rho}{\partial x_j \partial t}[\phi] - \frac{\partial^2 \rho u_i' u_j'}{\partial x_i \partial x_j}[\phi]\end{aligned} \tag{3.18}$$

By inserting this result into Eq. (3.17) the following is obtained

$$\begin{aligned}\frac{\partial^2 \rho}{\partial t^2}[\phi] + 2U_{j,0}\frac{\partial^2 \rho}{\partial x_j \partial t}[\phi] + U_{i,0}U_{j,0}\frac{\partial^2 \rho}{\partial x_j \partial x_i}[\phi] = &\left(\frac{\partial}{\partial t} + U_{j,0}\frac{\partial}{\partial x_j}\right) Q[\phi] \\ &- \frac{\partial}{\partial x_i}\tilde{L}_i[\phi] + U_{j,0}\frac{\partial}{\partial x_j}Q[\phi] \\ &+ \frac{\partial^2 \rho u_i' u_j'}{\partial x_i \partial x_j}[\phi] + \frac{\partial^2 p_{ij}}{\partial x_i \partial x_j}[\phi]\end{aligned} \tag{3.19}$$

In order to obtain a convective wave equation the identity in Eq. (3.16) is used to rewrite some of the terms Eq. (3.19). After this, $c_0^2 \frac{\partial^2 \rho'}{\partial x_i \partial x_i}[\phi]$ is subtracted from both sides to obtain the convective Ffowcs Williams-Hawkings equation for stationary, permeable surfaces

$$\Box^2 \rho'[\phi] = \left(\frac{\partial}{\partial t} + U_{j,0}\frac{\partial}{\partial x_j}\right) Q[\phi] - \frac{\partial}{\partial x_i}L_i[\phi] + \frac{\partial^2}{\partial x_i \partial x_j}T_{ij}[\phi] \tag{3.20}$$

Here, $\Box^2$ is the convective wave operator, $L_i[\phi]$ is a new source term and $T_{ij}[\phi]$ is the distribution generated by the Lighthill tensor. These terms are defined as follows

$$\begin{aligned} \Box^2 &= \frac{\partial^2}{\partial t^2} + 2U_{j,0}\frac{\partial^2}{\partial x_j \partial t} + U_{i,0}U_{j,0}\frac{\partial^2}{\partial x_j \partial x_i} - c_0^2 \frac{\partial^2}{\partial x_i \partial x_i} \\ L_i[\phi] &= \int_t \int_{\partial V} (\rho u_i'(U_{j,0} + u_j') + p'\delta_{ij} - \sigma_{ij}) n_j \phi dS dt \\ T_{ij}[\phi] &= (\rho u_i' u_j' + (p' - c_0^2 \rho')\delta_{ij} - \sigma_{ij})[\phi] \end{aligned} \tag{3.21}$$

It is emphasized that all terms in Eq. (3.20) are distributions, i.e. they represent integrals of some field multiplied by a test function. This equation can also be written in functional form, by omitting the integrals and the test functions and only writing out the underlying fields according to

$$\begin{aligned} \Box^2 \left[H(f)\rho'\right] = &\left(\frac{\partial}{\partial t} + U_{j,0}\frac{\partial}{\partial x_j}\right)\Big[\underbrace{(\rho(U_{0,i} + u_i') - \rho_0 U_{i,0})\, n_i}_{Q(\mathbf{x},t)}\,\delta(f)\Big] \\ &- \frac{\partial}{\partial x_i}\Big[\underbrace{(\rho u_i'(U_{j,0} + u_j') + p'\delta_{ij} - \sigma_{ij}) n_j}_{L_i(\mathbf{x},t)}\,\delta(f)\Big] \\ &+ \frac{\partial^2}{\partial x_i \partial x_j}\left[H(f) T_{ij}(\mathbf{x},t)\right] \end{aligned} \tag{3.22}$$

The delta functions appearing in this expression comes from the fact that a surface integral may be rewritten as a volume integral over $\mathbb{R}^3$ if the integrand is multiplied by $\delta(f)$, where f is a scalar field that is zero at the surface [26]. In Eq. (3.22) the functions corresponding to the distributions $Q[\phi]$ and $L_i[\phi]$ have also been defined. Equation (3.22) is equivalent to the convective Ffowcs Williams - Hawkings equation derived by Najafi-Yazidi et al. [30] if the integration surface is kept stationary in their equation. It should also be noted that the same convective Ffowcs Williams - Hawkings equations that was derived in this thesis has been derived earlier by Lockard [31] by performing a Galilean transformation of the original Ffowcs Williams - Hawkings equation.

3.2 Solution of the Convective Ffowcs Williams - Hawkings Equation

The solution to Eq. (3.22) is obtained by forming a convolution with a Green's function to the convective wave operator. If the ambient flow is assumed to be aligned with the

x_1 axis the Green's function takes on the following form [30]

$$\begin{aligned} G(\mathbf{x},t) =& \begin{cases} \frac{\delta(t-R(\mathbf{x})/c_0)}{4\pi c_0^2 R^*(\mathbf{x})} & t>0 \\ 0 & \text{else} \end{cases} \\ R(\mathbf{x}) =& \frac{-M_0 x_1 + R^*(\mathbf{x})}{\beta^2} \\ R^*(\mathbf{x}) =& \sqrt{x_1^2 + \beta^2(x_2^2+x_3^2)} \\ \beta =& \sqrt{1-M_0^2} \end{aligned} \tag{3.23}$$

This Green's function describes the solution to the convective wave equation for the case when the right hand side is a unit impulse in the origin at $t = 0$: $\delta(\mathbf{x})\delta(t)$. By examining the structure of Eq. (3.23) it can be seen that the response to this impulse is zero everywhere except when $R(\mathbf{x}) = c_0 t$. This condition is satisfied for all points on a sphere with radius $r = c_0 t$ and center at $x_1 = M_0 c_0 t$, representing the fact that the sound impulse is convected downstream with the flow while at the same time traveling radially outwards relative to the flow.

The convolution between Eq. (3.22) and (3.23) reads as follows

$$\begin{aligned} c_0^2\rho'(\mathbf{x},t) =& \left(\frac{\partial}{\partial t} + U_{1,0}\frac{\partial}{\partial x_1}\right)\int_{-\infty}^{t}\int_{\mathbb{R}^3} \frac{Q(\mathbf{y},\tau)\delta(f(\mathbf{y}))\delta(t-\tau-R(\mathbf{x}-\mathbf{y})/c_0)}{4\pi R^*(\mathbf{x}-\mathbf{y})} d^3\mathbf{y}d\tau \\ &- \frac{\partial}{\partial x_i}\int_{-\infty}^{t}\int_{\mathbb{R}^3} \frac{L_i(\mathbf{y},\tau)\delta(f(\mathbf{y}))\delta(t-\tau-R(\mathbf{x}-\mathbf{y})/c_0)}{4\pi R^*(\mathbf{x}-\mathbf{y})} d^3\mathbf{y}d\tau \\ &+ \frac{\partial^2}{\partial x_i \partial x_j}\int_{-\infty}^{t}\int_{\mathbb{R}^3} \frac{H(f(\mathbf{y}))T_{ij}(\mathbf{y},\tau)\delta(t-\tau-R(\mathbf{x}-\mathbf{y})/c_0)}{4\pi R^*(\mathbf{x}-\mathbf{y})} d^3\mathbf{y}d\tau \end{aligned} \tag{3.24}$$

Physically, the above equation expresses the density perturbation at position $\mathbf{x}$ and time t as an integral over all possible source positions $\mathbf{y}$ and emission times τ. The presence of the delta function in the integral will however restrict the integral at a position $\mathbf{y}$ to be evaluated at a single time instant $\tau_{\text{ret}} = t - R(\mathbf{x}-\mathbf{y})/c_0$. If $\mathbf{x}$ is taken to be the position of the observer then τ_{ret} represents the time when an acoustic signal generated at $\mathbf{y}$ reaches the observer at time t. Although it is not obvious from the notation in Eq. (3.24), the presence of $\delta(f)$ in the first two integrals will convert these volume integrals into a surface integral over ∂V [26]. In addition, the third integral is only non-zero outside of ∂V. This last observation implies that if ∂V is placed such that it encloses all relevant noise sources, T_{ij} will have a negligible amplitude outside of ∂V and the third integral can therefore be omitted. This simplification will be adopted for the remainder of this thesis.

The aim is now to convert the above argument into sound mathematical expressions. As a first step the order of integration is interchanged and the integral in τ is evaluated

to obtain

$$\begin{aligned} c_0^2\rho'(\mathbf{x},t) = &\left(\frac{\partial}{\partial t} + U_{1,0}\frac{\partial}{\partial x_1}\right)\int_{\mathbb{R}^3}\frac{Q(\mathbf{y},\tau_{\text{ret}})\delta(f(\mathbf{y}))}{4\pi R^*(\mathbf{x}-\mathbf{y})}d^3\mathbf{y} \\ &- \frac{\partial}{\partial x_i}\int_{\mathbb{R}^3}\frac{L_i(\mathbf{y},\tau_{\text{ret}}))\delta(f(\mathbf{y}))}{4\pi R^*(\mathbf{x}-\mathbf{y})}d^3\mathbf{y} \end{aligned} \tag{3.25}$$

The spatial derivatives can be moved inside the integrals in Eq. (3.25) since the integration boundaries does not depend on $\mathbf{x}$. If $h(\mathbf{y},\tau_{\text{ret}})$ is used to denote either Q or L_i this gives the following result

$$\begin{aligned} \frac{\partial}{\partial x_i}\left(\frac{h(\mathbf{y},\tau_{\text{ret}})}{R^*}\right) &= -\frac{\dot{h}(\mathbf{y},\tau_{\text{ret}})}{R^*c_0}\frac{\partial R}{\partial x_i} - \frac{h(\mathbf{y},\tau_{\text{ret}})}{R^{*2}}\frac{\partial R^*}{\partial x_i} \\ &= -\frac{\dot{h}(\mathbf{y},\tau_{\text{ret}})\tilde{R}_i}{R^*c_0} - \frac{h(\mathbf{y},\tau_{\text{ret}})\tilde{R}_i^*}{R^{*2}} \end{aligned} \tag{3.26}$$

Here, a dot represents a partial derivative with respect to the retarded time τ_{ret}. It should also be emphasized that the spatial dependency in the above equation was omitted for brevity, e.g. $R = R(\mathbf{x}-\mathbf{y})$. The new functions introduced in Eq. (3.26) are defined as follows [30]

$$\begin{aligned} &\tilde{R}_1(\mathbf{x}) = \frac{1}{\beta^2}\left(-M_0 + \tilde{R}_1^*(\mathbf{x})\right), \quad \tilde{R}_2(\mathbf{x}) = \frac{x_2}{R^*(\mathbf{x})}, \qquad \tilde{R}_3(\mathbf{x}) = \frac{x_3}{R^*(\mathbf{x})} \\ &\tilde{R}_1^*(\mathbf{x}) = \frac{x_1}{R^*(\mathbf{x})}, \qquad\qquad \tilde{R}_2^*(\mathbf{x}) = \beta^2\frac{x_2}{R^*(\mathbf{x})}, \quad \tilde{R}_3^*(\mathbf{x}) = \beta^2\frac{x_3}{R^*(\mathbf{x})} \end{aligned} \tag{3.27}$$

Bringing the time derivative under the integration sign is simpler since it holds true that

$$\frac{\partial}{\partial t}h(\mathbf{y},\tau_{\text{ret}}) = \dot{h}(\mathbf{y},\tau_{\text{ret}}) \tag{3.28}$$

By introducing Eq. (3.26) and (3.28) into Eq. (3.25) the following is obtained

$$\begin{aligned} c_0^2\rho'(\mathbf{x},t) = &+ \int_{\mathbb{R}^3}\frac{\dot{Q}(\mathbf{y},\tau_{\text{ret}})(1 - M_0\tilde{R}_1(\mathbf{x}-\mathbf{y}))}{4\pi R^*(\mathbf{x}-\mathbf{y})}\delta(f(\mathbf{y}))d^3\mathbf{y} \\ &- \int_{\mathbb{R}^3}\frac{Q(\mathbf{y},\tau_{\text{ret}})U_{1,0}\tilde{R}_1^*(\mathbf{x}-\mathbf{y})}{4\pi R^{*2}(\mathbf{x}-\mathbf{y})}\delta(f(\mathbf{y}))d^3\mathbf{y} \\ &+ \int_{\mathbb{R}^3}\frac{1}{c_0}\frac{\dot{L}_i(\mathbf{y},\tau_{\text{ret}})\tilde{R}_i(\mathbf{x}-\mathbf{y})}{4\pi R^*(\mathbf{x}-\mathbf{y})}\delta(f(\mathbf{y}))d^3\mathbf{y} \\ &+ \int_{\mathbb{R}^3}\frac{L_i(\mathbf{y},\tau_{\text{ret}})\tilde{R}_i^*(\mathbf{x}-\mathbf{y})}{4\pi R^{*2}(\mathbf{x}-\mathbf{y})}\delta(f(\mathbf{y}))d^3\mathbf{y} \end{aligned} \tag{3.29}$$

The volume integral is finally converted into a surface integral and some terms are rewrit-

ten slightly in order to obtain the following final formulation

$$\begin{aligned} p'_{\text{obs}}(\mathbf{x},t) = &+ \int_{\partial V} \frac{\dot{Q}(\mathbf{y},\tau_{\text{ret}})R(\mathbf{x}-\mathbf{y})}{4\pi R^{*2}(\mathbf{x}-\mathbf{y})} dS - \int_{\partial V} \frac{Q(\mathbf{y},\tau_{\text{ret}})U_{1,0}\tilde{R}_1^*(\mathbf{x}-\mathbf{y})}{4\pi R^{*2}(\mathbf{x}-\mathbf{y})} dS \\ &+ \int_{\partial V} \frac{1}{c_0} \frac{\dot{L}_i(\mathbf{y},\tau_{\text{ret}})\tilde{R}_i(\mathbf{x}-\mathbf{y})}{4\pi R^*(\mathbf{x}-\mathbf{y})} dS + \int_{\partial V} \frac{L_i(\mathbf{y},\tau_{\text{ret}})\tilde{R}_i^*(\mathbf{x}-\mathbf{y})}{4\pi R^{*2}(\mathbf{x}-\mathbf{y})} dS \end{aligned} \tag{3.30}$$

Note that all integrals in this expression should be evaluated with respect to $\mathbf{y}$.

Equation (3.30) has been implemented into a Python program which was used in Paper B to calculate the far field noise signature of a CROR. Details on the numerical implementation as well as a discussion on the choice of the integration surface and the strength and potential weaknesses of the chosen formulation are also provided in this paper.

4 Summary of Papers

4.1 Paper A

D. Lindblad and N. Andersson. "Validating the Harmonic Balance Method for Turbomachinery Tonal Noise Predictions". *55th AIAA Aerospace Sciences Meeting.* AIAA Paper 2017-1171. Grapevine, TX, 9-13 January 2017

Motivation and Division of Work

The work reported in this paper aimed at validating the implementation of the Harmonic Balance method in G3D::Flow on two benchmark cases relevant for turbomachinery tonal noise prediction codes. The second benchmark problem also allowed the phase shifted periodic boundary condition that was added to G3D::Flow together with the Harmonic Balance method for performing simulations with only one blade per row to be validated. The implementation of the Harmonic Balance solver and phase shifted periodic boundary condition was performed by Daniel with the support of Niklas. The way that the gust boundary condition was implemented was invented by Niklas. Meshing, setting up the simulations, post processing results and writing the paper was done by Daniel.

Results and Conclusion

The first benchmark case consisted of calculating the acoustic response of an isolated airfoil when subjected to vortical velocity gusts. In general, the Harmonic Balance method implemented in G3D::Flow showed very good agreement when compared to other published results both in terms of the RMS pressure response on the airfoil surface as well as the far field noise directivity. In the second benchmark case the acoustic response of a two dimensional outlet guide vane (OGV) due to incoming velocity gusts was calculated. This case was found to be more challenging than the first one, which in part was due to the lack of higher order nonreflecting boundary conditions in G3D::Flow. This necessitated the use of an extended domain downstream of the OGV in which a buffer zone was employed. Despite these limitations, good agreement was obtained when comparing the RMS pressure on the OGV with other published results. This case also demonstrated that the phase shifted periodic boundary condition worked as intended. It should finally be noted that the cases investigated in this paper all were linear in nature, so aliasing is not believed to have been an issue.

4.2 Paper B

D. Lindblad et al. "Aeroacoustic Analysis of a Counter Rotating Open Rotor based on the Harmonic Balance Method". *2018 AIAA Aerospace Sciences Meeting.* AIAA Paper 2018-1004. Kissimmee, FL, 8-12 January 2018

Motivation and Division of Work

The work reported in this paper aimed at demonstrating the complete computational framework developed in this thesis for predicting the noise signature of a full scale CROR in flight. Two things were added to the framework in this work, namely a mode matching bladerow interface and the acoustic analogy based on the convective form of the Ffowcs Williams - Hawkings equation for permeable surfaces. The bladerow interface was implemented by Daniel and Gonzalo. The acoustic analogy was implemented and validated by Daniel. Niklas provided a great deal of technical support on both the aforementioned subjects along the way. The CROR geometry used was designed by Alex and later meshed by Gael and Suk-kee at ISAE. Setup of the simulations, post processing results and writing the paper was done by Daniel.

Results and Conclusion

The validation of the implemented acoustic analogy showed that the selected formulation gave excellent agreement with analytical solutions for monopole and dipole noise radiation in uniformly moving media. When the acoustic analogy was later applied to the CROR, spurious oscillations was observed in the noise directivity plots. Some investigation led the authors to believe that the root of the problem was that spurious signals were generated at the integration surface behind the rear rotor when the rotor wakes crossed the surface. The results also showed that the complete framework was capable of simulating the unsteady flow field around a CROR, but so far no complete validation has been possible due to the lack of reference data.

5 Concluding Remarks

In this work a computational framework for predicting the aerodynamic tonal noise generated by the propulsion unit of a Counter Rotating Open Rotor (CROR) has been presented. The framework models the noise generating mechanisms by solving the Favre-Averaged Navier Stokes equations using the Finite Volume method for spatial discretization and the Harmonic Balance method for temporal discretization [13]. This solution is then coupled to an acoustic analogy which calculates the far field noise signature of the CROR by solving a convective form of the Ffowcs Williams - Hawkings equation for permeable sampling surfaces in uniformly moving media [9, 30]. In Paper A the Harmonic Balance method was shown to accurately predict the noise caused by unsteady interaction between a vortical gust and airfoil geometry. This type of noise is relevant for a CROR since the wakes generated by the upstream fan blades impinge on the downstream fan blades, causing what is often referred to as interaction noise [10]. In Paper B the complete framework was demonstrated on a full scale CROR and the chosen acoustic analogy was validated for generic monopole and dipole noise sources situated in a moving media.

Several challenges that should be addressed in future work was identified throughout this work. With regards to the Harmonic Balance method the most important question to be answered is which number of unsteady harmonics that are necessary in order to incorporate all the relevant unsteady effects in the simulation. This issue becomes even more prominent when it is considered that a low number of harmonics may result in that the solution becomes contaminated by aliasing. This implies that even if one only is interested in the lower harmonics, one may be forced to include a larger amount of harmonics in the simulation just to keep the ones of interest alias free, as was done by Olausson [12]. Oversampling in conjunction with zero padding of the higher frequencies was further done by Frey et al. [16]. Additional damping, similar to a subgrid scale model used in LES, could also potentially solve the alias issue, but the design of such a model was out of scope for this thesis. A simpler approach would be to perform a mode convergence study in order to establish a sufficient number of harmonics necessary for a particular application.

Another challenge that was identified in Paper B was the placement of the integration surface used for the acoustic analogy as well as the choice of the underlying formulation implemented. In general, a porous integration surface should be placed so that it encapsulates all relevant noise sources [32, 28]. This may be challenging for a CROR when strong shocks extend far away from the blade surfaces since the grid typically is coarsened away from the CROR to save computational cost, which in turn yields poor input to the acoustic analogy if the integration surface is located in the coarse mesh region. The same issue holds if one attempts to move the integration surface further downstream in order to let the rotor wake mix out further and avoid the potential problems associated with the blade wake crossing the integration surface. Recent work reported in the literature appear to address the wake related issue by reformulating the underlying equations [33], but it remains an open question whether this solves the issue encountered in this work.

Further work on boundary conditions and the mode matching rotor-rotor interface is also needed in order to improve the absorbing features of the boundaries/interface

beyond 1D characteristics that have been employed thus far. The aim of future work is to extend the mode matching interface as well as inlet/outlet boundaries to absorb 2D modes based on the theory of Giles [34, 35], Saxer and Giles [36] and Kersken et al. [37].

Despite the aforementioned challenges it is the authors opinion that the Harmonic Balance method in conjunction with an acoustic analogy based on the Ffowcs Williams - Hawkings equations is a very appealing method for predicting the tonal noise generated by unducted propulsors in particular, and turbomachinery blades in general. Specifically, the Harmonic Balance method lends itself well to be used with phase shifted periodic boundary conditions [38], unsteady higher order nonreflecting boundary conditions [39] and steady state acceleration techniques such as GMRES and Implicit Residual Smoothing [12].

References

[1] D. Lindblad and N. Andersson. "Validating the Harmonic Balance Method for Turbomachinery Tonal Noise Predictions". *55th AIAA Aerospace Sciences Meeting*. AIAA Paper 2017-1171. Grapevine, TX, 9-13 January 2017.

[2] D. Lindblad et al. "Aeroacoustic Analysis of a Counter Rotating Open Rotor based on the Harmonic Balance Method". *2018 AIAA Aerospace Sciences Meeting*. AIAA Paper 2018-1004. Kissimmee, FL, 8-12 January 2018.

[3] Airbus S.A.S. *Global Market Forecast 2017-2036*. Accessed online at `www.airbus.com` (2018-02-23). AIRBUS S.A.S., 2017. ISBN: 978-2-9554382-2-6.

[4] International Civil Aviation Organization. *ICAO Environmental Report 2016*. Accessed online at `www.icao.int` (2018-02-23). International Civil Aviation Organization, 2016.

[5] European Commission. *FlightPath 2050*. Accessed online at `www.ec.europa.eu` (2018-02-23). European Union, 2011. ISBN: 978-92-79-19724-6.

[6] Advisory Council for Aviation Research and Innovation in Europe. *Strategic Research and Innovation Agenda - 2017 Update - Volume 1*. Accessed online at `www.acare4europe.org` (2018-02-23). Advisory Council for Aviation Research and Innovation in Europe, 2017.

[7] M. J. Lighthill. On Sound Generated Aerodynamically. I. General Theory. *Proceedings of the Royal Society of London. Series A, Mathematical and Physical Sciences* **211**.1107 (Mar. 1952), 564–587.

[8] M. J. Lighthill. On Sound Generated Aerodynamically. II. Turbulence as a Source of Sound. *Proceedings of the Royal Society of London. Series A, Mathematical and Physical Sciences* **222**.1148 (Feb. 1954), 1–32.

[9] J. E. Ffowcs Williams and D. L. Hawkings. Sound Generation by Turbulence and Surfaces in Arbitrary Motion. *Philosophical Transactions of the Royal Society of London. Series A, Mathematics and Physical Sciences* **264**.1151 (May 1969), 321–342.

[10] H. H. Hubbard, ed. *Aeroacoustics of Flight Vehicles. Theory and Practice*. Vol. 1. Noise Sources. Acoustical Society of America, 1995. ISBN: 1-56396-404-X.

[11] N. Andersson. "A Study of Subsonic Turbulent Jets and Their Radiated Sound Using Large-Eddy Simulation". PhD thesis. Gothenburg, Sweden: Division of Fluid Dynamics, Department of Applied Mechanics, Chalmers University of Technology, 2005. ISBN: 91-7291-679-6.

[12] M. Olausson. "Turbomachinery Aeroacoustic Calculations using Nonlinear Methods". PhD thesis. Gothenburg, Sweden: Division of Fluid Dynamics, Department of Applied Mechanics, Chalmers University of Technology, 2011. ISBN: 978-91-7385-481-8.

[13] K. C. Hall, P. T. Jeffrey, and W. S. Clark. Computation of Unsteady Nonlinear Flows in Cascades Using a Harmonic Balance Technique. *AIAA Journal* **40**.5 (May 2002), 879–886.

[14] K. Ekici and K. C. Hall. Nonlinear Analysis of Unsteady Flows in Multistage Turbomachines Using Harmonic Balance. *AIAA Journal* **45**.5 (May 2007), 1047–1057.

[15] K. Ekici and K. C. Hall. Nonlinear Frequency-Domain Analysis of Unsteady Flows in Turbomachinery with Multiple Excitation Frequencies. *AIAA Journal* **46**.8 (Aug. 2008), 1912–1920.

[16] C. Frey et al. "A Harmonic Balance Technique for Multistage Turbomachinery Applications". *ASME Turbo Expo 2014: Turbine Technical Conference and Exposition*. GT2014-25230. Dsseldorf, Germany, 16-20 June 2014.

[17] G. B. Folland. *Fourier Analysis and Its Applications*. Vol. 4. American Mathematical Society, 1992. ISBN: 978-0-8218-4790-9.

[18] A. K. Gopinath and A. Jameson. "Application of the Time Spectral Method to Periodic Unsteady Vortex Shedding". *44th AIAA Aerospace Sciences Meeting and Exhibit*. AIAA Paper 2006-0449. Reno, NV, 9-12 January 2006.

[19] K. Holmker. *Linjr Algebra med Tillmpningar*. Gothenburg, Sweden: Department of Mathematics, Chalmers University of Technology and Gothenburg University, 1994.

[20] C. Hirsch. *Numerical Computation of Internal and External Flows. The Fundamentals of Computational Fluid Dynamics*. 2nd ed. Vol. 1. Butterworth-Heinemann, June 2007. ISBN: 978-0-7506-6594-0.

[21] H. Huang and K. Ekici. Stabilization of High-Dimensional Harmonic Balance Solvers Using Time Spectral Viscosity. *AIAA Journal* **52**.8 (Aug. 2014), 1784–1794.

[22] N. C. Gentilli. "Efficient Solution of Unsteady Nonlinear Flows Using a Multiple Zone Harmonic Balance Technique". MA thesis. Durham, NC: Department of Mechanical Engineering and Materials Science, Duke University, Dec. 2010.

[23] K. C. Hall et al. Harmonic Balance Methods Applied to Computational Fluid Dynamics Problems. *International Journal of Computational Fluid Dynamics* **27**.2 (Jan. 2013), 52–67.

[24] J. G. Charney, R. Fjrtoft, and J. Von Neumann. Numerical Integration of the Barotropic Vorticity Equation. *Tellus* **2**.4 (1950), 237–254.

[25] N. Curle. The Influence of Solid Boundaries upon Aerodynamic Sound. *Proceedings of the Royal Society of London. Series A, Mathematical and Physical Sciences* **231**.1187 (Sept. 1955), 505–514.

[26] F. Farassat. *Introduction to Generalized Functions With Applications in Aerodynamics and Aeroacoustics*. Technical Paper NASA-TP-3428. Corrected Copy. Hampton, VA: NASA, Apr. 1996.

[27] L. Debnath and P. Mikusiski. *Introduction to Hilbert Spaces. With Applications*. 3rd ed. Academic Press, Sept. 2005. ISBN: 9780122084386.

[28] P. di Francescantonio. A New Boundary Integral Formulation for the Prediction of Sound Radiation. *Journal of Sound and Vibration* **202**.4 (May 1997), 491–509.

[29] F. Farassat. *Derivation of Formulations 1 and 1A of Farassat*. Technical Report NASA/TM-2007-214853. Hampton, VA: NASA, Mar. 2007.

[30] A. Najafi-Yazidi, G. A. Brs, and L. Mongeau. An Acoustic Analogy Formulation for Moving Sources in Uniformly Moving Media. *Proceedings of the Royal Society A, Mathematical, Physical and Engineering Sciences* **467**.2125 (Jan. 2011), 144–165.

[31] D. P. Lockard. "A Comparison of Ffowcs Williams-Hawkings Solvers for Airframe Noise Predictions". *8th AIAA/CEAS Aeroacoustics Conference*. AIAA Paper 2002-2580. Breckenridge, CO, 17-19 June 2002.

[32] F. Farassat. *Open Rotor Noise Prediction at NASA Langley - Capabilities, Research and Development*. Technical Report NASA/TM-2010-216178. Hampton, VA: NASA, Jan. 2010.

[33] S. Zhong and X. Zhang. A sound extrapolation method for aeroacoustics far-field prediction in presence of vortical waves. *Journal of Fluid Mechanics* **820** (June 2017), 424–450.

[34] M. B. Giles. Nonreflecting Boundary Conditions for Euler Equation Calculations. *AIAA Journal* **28**.12 (Dec. 1990), 2050–2058.

[35] M. B. Giles. "Non-Reflecting Boundary Conditions for the Euler Equations". *CFDL-TR-88-1*. Feb. 1988.

[36] A. P. Saxer and M. B. Giles. Quasi-Three-Dimensional Nonreflecting Boundary Conditions for Euler Equations Calculations. *Journal of Propulsion and Power* **9**.2 (Mar. 1993), 263–271.

[37] H.-P. Kersen et al. "Nonreflecting Boundary Conditions for Aeroelastic Analysis in Time and Frequency Domain 3D RANS Solvers". *ASME Turbo Expo 2014: Turbine Technical Conference and Exposition*. GT2014-25499. Dsseldorf, Germany, 16-20 June 2014.

[38] G. A. Gerolymos, G. J. Michon, and J. Neubauer. Analysis and Application of Chorochronic Periodicity in Turbomachinery Rotor/Stator Interaction Computations. *Journal of Propulsion and Power* **18**.6 (Nov. 2002), 1139–1152.

[39] C. Frey, G. Ashcroft, and H.-P. Kersen. "Simulations of Unsteady Blade Row Interactions Using Linear and Non-Linear Frequency Domain Methods". *ASME Turbo Expo 2015: Turbine Technical Conference and Exposition*. GT2015-43453. Montral, Canada, 15-19 June 2015.